NASA/CR-2007-214889

Velocity-Field Measurements of an Axisymmetric Separated Flow Subjected to Amplitude-Modulated Excitation

Barry James Trosin
Michigan State University, East Lansing, Michigan

July 2007

The NASA STI Program Office . . . in Profile

Since its founding, NASA has been dedicated to the advancement of aeronautics and space science. The NASA Scientific and Technical Information (STI) Program Office plays a key part in helping NASA maintain this important role.

The NASA STI Program Office is operated by Langley Research Center, the lead center for NASA's scientific and technical information. The NASA STI Program Office provides access to the NASA STI Database, the largest collection of aeronautical and space science STI in the world. The Program Office is also NASA's institutional mechanism for disseminating the results of its research and development activities. These results are published by NASA in the NASA STI Report Series, which includes the following report types:

- TECHNICAL PUBLICATION. Reports of completed research or a major significant phase of research that present the results of NASA programs and include extensive data or theoretical analysis. Includes compilations of significant scientific and technical data and information deemed to be of continuing reference value. NASA counterpart of peer-reviewed formal professional papers, but having less stringent limitations on manuscript length and extent of graphic presentations.

- TECHNICAL MEMORANDUM. Scientific and technical findings that are preliminary or of specialized interest, e.g., quick release reports, working papers, and bibliographies that contain minimal annotation. Does not contain extensive analysis.

- CONTRACTOR REPORT. Scientific and technical findings by NASA-sponsored contractors and grantees.

- CONFERENCE PUBLICATION. Collected papers from scientific and technical conferences, symposia, seminars, or other meetings sponsored or co-sponsored by NASA.

- SPECIAL PUBLICATION. Scientific, technical, or historical information from NASA programs, projects, and missions, often concerned with subjects having substantial public interest.

- TECHNICAL TRANSLATION. English-language translations of foreign scientific and technical material pertinent to NASA's mission.

Specialized services that complement the STI Program Office's diverse offerings include creating custom thesauri, building customized databases, organizing and publishing research results ... even providing videos.

For more information about the NASA STI Program Office, see the following:

- Access the NASA STI Program Home Page at ***http://www.sti.nasa.gov***

- E-mail your question via the Internet to help@sti.nasa.gov

- Fax your question to the NASA STI Help Desk at (301) 621-0134

- Phone the NASA STI Help Desk at (301) 621-0390

- Write to:
  NASA STI Help Desk
  NASA Center for AeroSpace Information
  7115 Standard Drive
  Hanover, MD 21076-1320

NASA/CR-2007-214889

Velocity-Field Measurements of an Axisymmetric Separated Flow Subjected to Amplitude-Modulated Excitation

Barry James Trosin
Michigan State University, East Lansing, Michigan

National Aeronautics and
Space Administration

Langley Research Center
Hampton, Virginia 23681-2199

Prepared for Langley Research Center
under Grant NNL05AA11H

July 2007

Available from:

NASA Center for AeroSpace Information (CASI)
7115 Standard Drive
Hanover, MD 21076-1320
(301) 621-0390

National Technical Information Service (NTIS)
5285 Port Royal Road
Springfield, VA 22161-2171
(703) 605-6000

ABSTRACT

VELOCITY-FIELD MEASUREMENTS OF AN AXISYMMETRIC SEPARATED FLOW SUBJECTED TO AMPLITUDE-MODULATED EXCITATION

By

Barry James Trosin

Active flow control was applied at the point of separation of an axisymmetric, backward-facing-step flow. The control was implemented by employing a Helmholtz resonator that was externally driven by an amplitude–modulated, acoustic disturbance from a speaker located upstream of the wind tunnel. The velocity field of the separating/reattaching flow region downstream of the step was characterized using hotwire velocity measurements with and without flow control.

Conventional statistics of the data reveal that the separating/reattaching flow is affected by the imposed forcing. Triple decomposition along with conditional averaging was used to distinguish periodic disturbances from random turbulence in the fluctuating velocity component. The outcome of this analysis showed that the forcing triggered large-scale, organized structures that formed at regular intervals near the separation point. The structures convect downstream and grow to a size comparable to the step height at a location approximately half way to reattachment. A significant outcome of the present study is that it demonstrates that amplitude-modulated forcing of the separated flow alters the flow in the same manner as the more conventional method of periodic excitation.

TABLE OF CONTENTS

1 Introduction 1

1.1 Background 1

1.2 Motivation 5

1.3 Objectives 6

1.4 References 8

2 Experimental Setup 10

2.1 Wind Tunnel and Facility 10

2.2 Axisymmetric Backward Facing Step Model 12

2.3 Data Acquisition Systems 21

2.4 Experimental Procedure 27

2.5 References 41

3 Conventional-statistics Results and Discussion 42

3.1 Mean Velocity 42

3.2 Fluctuating Velocity 45

3.3 Velocity Probability Density Function 55

3.4 References 58

4 Conditional-average Results and Discussion 59

4.1 Conditional averaging 59

4.2 Triple decomposition 70

4.3 References 84

5 Conclusions and Recommendations for Future Work 85

5.1 Conclusions 85

5.2 Future Work 87

5.3 References 88

A. Appendix 89

LIST OF TABLES

Table 2.1 Function generator settings for the forcing signal 31

LIST OF FIGURES

Figure 1.1 A Schematic drawing illustrating the geometry and some flow features of the separated flow over a backward-facing step 2

Figure 2.1 Schematic of wind tunnel (demission in meters) 10

Figure 2.2 Schematic of the axisymmetric backward-facing-step model (dimensions in m) 13

Figure 2.3 Cross section of the measurement region downstream of the back step (flow is out of the paper) 15

Figure 2.4. Cross section drawing of the resonator and step region (note drawing is not to scale; dimensions in mm) 16

Figure 2.5 Geometry of the resonator's outer shell supports (dimensions in mm) 17

Figure 2.6 Location of the speaker used to drive the resonator relative to the wind tunnel (dimensions in meters) 18

Figure 2.7 Example of an amplitude-modulated sine wave with MI = 2/3 21

Figure 2.8 Picture of Hotwire Traverse System 25

Figure 2.9 Sample image of the hotwire above model wall during positioning procedure 27

Figure 2.10 Location of hotwire for carrier frequency determination 30

Figure 2.11 Amplitude modulated resonator's jet velocity 31

Figure 2.12 Hotwire trace of the flow velocity above the resonator's slit..... 32

Figure 2.13 Forced- and unforced-flow mean-pressure profiles downstream of the step 35

Figure 2.14 Sample Hotwire calibration curves 37

Figure 2.15 Forward flow probability from PIV measurements of Hudy (color map); and hotwire measurement locations for the present investigation (black dots)..... 38

Figure 3.1 Normalized mean-velocity plots..... 43

Figure 3.2 Normalized mean-velocity profiles at selected x/h locations..... 45

Figure 3.3 Normalized turbulent-velocity rms contour plots..... 46

Figure 3.4 Normalized turbulent-velocity rms profiles at selected x/h locations 48

Figure 3.5 Peak q'_{rms} location at different streamwise positions 49

Figure 3.6 Streamwise evolution of the maximum q'_{rms} values 50

Figure 3.7 Power spectral density of q' for the unforced flow at selected x/h locations .. 51

Figure 3.8 Power spectral density of q' for the forced flow at selected x/h locations 52

Figure 3.9 Power spectral density of q' for the unforced flow at Selected x/h Locations (broken line shows sub-harmonic of the forcing frequency) 54

Figure 3.10 Power spectral density for the forced flow at selected x/h locations (broken

line shows sub-harmonic of the forcing frequency) 55

Figure 3.11 Velocity properties at y/h = 0.6833 and x/h = 1.5: (a) sample velocity trace for unforced case, (b) sample velocity trace for forced case, (c) PDF's..... 56

Figure 4.1 Sample time series illustrating different forcing-cycle phases for conditional averaging: (a) forcing signal; (b) flow velocity 60

Figure 4.2 Conditional-average-velocity contour plots at selected phases of the forcing cycle 63

Figure 4.3 Close up of the conditional-average-velocity contour plots in the vicinity of the separation point 65

Figure 4.4 Geometry of Greenblatt's hump model and PIV measurement locations..... 66

Figure 4.5 Phase-averaged $<q^2>$ contours: comparison of present results with those calculated from Greenblatt's[3] data at selected phases 68

Figure 4.6 Comparison of $<U^2>$and $<q^2>$ contours at $\varphi = 0°$ calculated from Greenblatt's data 70

Figure 4.7 Contours of the conditional vorticity, and energy of the streamwise turbulent velocity component, computed from Greenblatt's data for selected phases of the forcing cycle..... 73

Figure 4.8 $<\hat{q}^2>$ contours for selected phases of the forcing cycle 76

Figure 4.9 Streamwise location of the peak of $<\hat{q}^2>$ at different phases of the forcing

cycle. Straight lines represent least-squares fits used to calculate the convection velocity..... 78

Figure 4.10 q̃ contour plots for selected phases of the forcing cycle..... 81

Figure 4.11 rms of the turbulent (top) and the organized (bottom) velocity components. Broken white line identifies the center of the shear layer based on peak q'_{rms} 83

(Images in this thesis are presented in color.)

NOMENCLATURE

Symbol	Definition
A	empirical hotwire calibration constant
A_1	amplitude setting of function generator one
A_2	amplitude setting of function generator two
A_m	amplitude of amplitude-modulated signal
A_{me}	peak amplitude of modulation envelope
B	empirical hotwire calibration constant
c	chord length
C_μ	oscillatory-control momentum-based forcing coefficient
C_p	mean-pressure coefficient
d	slot width of resonator
E	hotwire voltage
F	frequency
F^+	reduced excitation frequency
$F(t)$	amplitude modulated signal

f_c	carrier frequency
f_m	modulation frequency
h	step height
m	amplitude of modulation frequency
M	number of forcing cycles in a time series
MI	modulation index
N	total number of data points in a time series
n	time shift or delay
P_r	mean reference pressure
P_s	mean surface pressure
q	velocity magnitude
$\overline{q}$	time-averaged velocity magnitude
q'	fluctuating component of velocity magnitude
$\tilde{q}$	organized-motion velocity magnitude
$\hat{q}$	turbulent-motion velocity magnitude
Re_c	Reynolds number based on chord length

Re_h	Reynolds number based on step height
Re_t	Reynolds number based on model height
rms	root mean square
t	time
t_o	time variable for phase averaging
U_∞	freestream velocity
u	streamwise velocity component
$\|u\|$	absolute value of streamwise velocity component
$\hat{u}$	turbulent-motion streamwise velocity component
$u_{j,rms}$	rms jet velocity
v	wall-normal velocity component
x	streamwise coordinate
x_r	mean reattachment length
y	wall-normal coordinate
ρ	density of air
φ	phase of forcing signal

$\varphi_{q'q'}$	power spectrum of q'
τ	period of forcing signal
ω	spanwise vorticity
$\langle\ \rangle$	denotes phase averaging

1 Introduction

1.1 Background

Within the field of fluid dynamics, there are many areas that are still not completely understood, one such area is separated flows. Separated flows naturally occur in many situations: over airfoils at high angle of attack, in turbines, in dump combustors, and in many other applications. Therefore, there have been many studies of the physics of separated flows. Some have investigated the unsteady wall-pressure signature generated by the turbulent flow structures; others have utilized velocity field measurements to gain an understanding of the flow features. A simplified (canonical) version of a separated flow is that over a backward-facing step; a generic sketch of the geometry and some flow features can be seen in Figure 1.1. For this geometry, the flow separates at the step and creates a shear layer that reattaches at some location farther downstream (on average), denoted as x_r. A mean separation streamline can be drawn from the point of separation at the edge of the step to the point of reattachment at x_r. Beneath the separation streamline, there is a primary and secondary recirculation zones (see Figure 1.1).

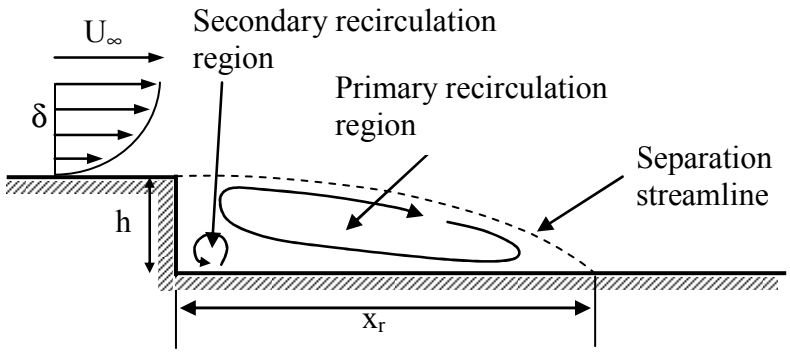

Figure 1.1 A Schematic drawing illustrating the geometry and some flow features of the separated flow over a backward-facing step

Over the years, a large number of researchers tried to control the size of the separation region or eliminate it all together when possible. Many methods have been tried to control the separation region, the most prominent of which are: steady suction, steady blowing, and unsteady excitation. Steady suction is a technique that is employed through either a slot at the point of separation or through a series of slots and/or holes in the separation region. Through these orifices, fluid is removed from the low-speed region just above the surface to deflect higher-speed fluid from farther above closer to the surface. The mass removal was believed to be the mechanism that causes the size of the separation bubble to decrease. This idea was first realized by Prandtl[1] (As sited by Greenblatt and Wygnanski[2]) and later tested by many individuals, which can be seen from the extensive research presented in the text book edited by Lachmann[3], and is still being investigated today. These studies have resulted in the realization that momentum, rather than mass, transfer as suggested earlier, was the mechanism that caused the flow control. This led to separation control via steady blowing whereby momentum is added to the low-speed fluid near the surface by steady blowing through a slot at the point of separation. This idea was vastly studied and was even put into production on a few

aircrafts; however, the cost and weight of the necessary plumbing and compressors to implement the technique greatly limited its effectiveness.

The importance of unsteady[1] (also termed periodic, or oscillatory) excitation was first realized by Schubauer and Skramstad[4] who introduced periodic excitation to trigger a known instability in a laminar boundary layer. This instability was theorized as a means to control transition from laminar to turbulent regimes. It was thought that periodic excitation would not be effective if applied to turbulent flows because of the inherent randomness of turbulence. However, experiments by Winant and Browand[5] showed the existence of large coherent structures in a turbulent mixing layer. By using harmonic excitation, Katz *et. al*.[6] was able to trigger the development of these large structures and was ultimately successful in attaching a turbulent mixing layer to a deflected flap.

Some recent investigations employed "synthetic jets" as the means of unsteady excitation. The jets are produced by internal actuators that are embedded in a cavity behind a slot that is located near or at the point of separation. Periodic oscillation of these actuators (typically a piezoelectric membrane, speaker, or compression driver) produces a strong, unsteady jet through the slot at the oscillation frequency. Sigurdson[7] conducted an investigation that implemented periodic forcing at the point of separation over a flat-faced cylinder that was aligned with its axis parallel to the freestream direction. He surmised that the mechanism causing the flow control was the generation

---

[1] There are numerous studies of oscillatory control of flows. Only a handful studies are selected for the present summary in order to highlight basic knowledge in the field that is relevant to the present work.

of large-scale vortex structures that produced a higher rate of entrainment and enhanced momentum transfer towards the separated flow region. This idea of the periodic forcing producing regular, downstream-convecting vortical structures is widely accepted at present.

Greenblatt *et. al.*[8] conducted an investigation of the flow over a wall-mounted "hump" that simulated a deflected flap portion of an airfoil, and employed periodic forcing. Through particle image velocimetry (PIV) measurements they were able to verify the existence of the large, downstream-convecting vortical structures and determine an optimal forcing frequency for the geometry.

Amitay and Glezer[9] and Glezer *et. al.*[10] performed research on a stalled, symmetric airfoil that employed periodic forcing at the leading edge. They found that for the traditional selection of control frequency, what they termed "order 1" forcing frequency ($F^+ \approx O(1)$; where F^+ is defined below), that a wake mode instability is triggered in the shear layer which generates the large-scale vortex shedding seen in previous studies, where

$$F^+ = \frac{fL}{U_\infty} \tag{1.1}$$

and f is the forcing frequency, L is a characteristic length of the separation region and U_∞ is the freestream velocity. However, it was found that if the forcing frequency is increased by an order of magnitude, $F^+ \approx O(10)$, then the wake instability is no longer triggered. Surprisingly, the flow stayed fully attached to the surface of the airfoil under the high-frequency forcing. The exact flow mechanism that caused the flow to remain

attached in this case is still unknown. Interestingly, Amitay and Glezer[9] and Glezer *et. al.*[10] suggest that for the high-frequency control, the control is insensitive to the particular choice of forcing frequency, as long as at it is above a certain threshold.

An alternative method of forcing was presented by Wiltse and Glezer[11] who used piezoelectric actuators at the downstream end of a square tube to excite the shear layer of an air jet issuing from the tube. The piezoelectric actuators were driven with an amplitude-modulated signal rather than the traditional periodic signal used in most flow-control investigations. Using this new actuation method they were able to modify the shear flow. Wiltse and Glezer[11] attributed their success to a flow non-linearity that generates line vortices that affect the flow. The approach of Wiltse and Glezer[11] requires high-level of forcing for the flow-nonlinearity to "kick in" and demodulate the excitation disturbance. As will become clear, this is different than the approach used here, where non-linearity of the excitation device, rather than the flow, renders the approach feasible. In this case it is possible to excite the flow with low-level disturbance.

1.2 Motivation

The current study follows a sequence of investigations performed on an axisymmetric, backward-facing-step geometry at Michigan State University in the Flow Physics and Control laboratory. Li developed a new, oscillating hotwire technique for measuring the magnitude and direction of the streamwise, wall-shear stress. He employed this technique to obtain single- and two-point wall-shear measurements beneath the axisymmetric separation bubble. Hudy[12] performed simultaneous wall-pressure and PIV measurements on the model under natural conditions. She found that vortex structures

with a scale of the order of the step height were intermittently generated by the roll-up of the separating shear layer at a location approximately half way to the mean reattachment point, then accelerated to a terminal convection velocity farther downstream. This offered a different view than the classical one of the vortex structures growing in size as they convect downstream. Later, experiments were conduced by Aditjandra[13] who developed a forcing system to produce an unsteady jet at the point of separation to control the flow. The jet was created by externally driving a Helmholtz resonator using a speaker upstream of the wind tunnel that is operating at the resonator's resonant frequency. To excite the flow at the desired frequency, which was much lower then the device's resonance frequency, the resonator was driven by an amplitude-modulated signal to generate the lower-frequency disturbance. Details of this forcing system, along with forcing parameters are described in chapter 2. Using the amplitude-modulated forcing, Aditjandra was able to successfully reduce the size of the separation region. He also investigated the space-time character of the wall-pressure signature using a 15-microphone array. However, Aditjandra's study did not provide information concerning the velocity field. Therefore, it is not clear whether the amplitude-modulated forcing produces the same changes in the flow field as conventional, periodic forcing, or a totally different flow-control mechanism is at play.

1.3 Objectives

- Characterize the flow field downstream of the point of separation on the axisymmetric, backward-facing-step model used by Li, Hudy and Aditjandra, using a single hotwire. The characterization is to be done for forced and

unforced-flow conditions, where the former is achieved utilizing the amplitude-modulated forcing approach developed by Aditjandra.

- Compare the velocity field under forced and unforced conditions, using conventional and conditional statistics to investigate the mechanism leading to flow control.

- Compare the current study to traditional periodic forcing.

1.4 References

[1] Prandtl L., "Über Flüssigkeitsbewenng bei sehr kleiner-Reibung" Proceedings of Third International Mathematical Congress, Heidelberg, 1904, pp. 484-491.

[2] Greenblatt, D., Wygnanski, I., "The Control of Flow Separation by Periodic Excitation" Progress in Aerospace, Vol. 36, 2000, pp. 487-545.

[3] Lachmann, G. V., "Boundary Layer Control. Its Principles and Applications" Vol. 1 New York Pergamon Press 1961.

[4] Schubauer, G. B., and Skramstad, H. K., "Laminar Boundary Layer Oscillations and Transitions on a Flat Plate" NACA Report 909, 1948.

[5] Winant, C.D., and Browand, F. K., "Vortex Pairing: the Mechanism of Turbulent Mixing-layer Growth at Moderate Reynolds Number" Journal of Fluid Mechanics, Vol. 63, 1974, pp. 237-255.

[6] Katz, Y., Nishri, B., Wygnanski, I., "The Delay of Turbulent Boundary Layer Separation by Oscillatory Active Control" Physics of Fluids, Vol. 1, 1989, pp. 179-181.

[7] Sigurdson, L. W., "The Structure and Control of a Turbulent Reattaching Flow", Journal of Fluid Mechanics. Vol. 298, 1999, pp. 139-165.

[8] Greenblatt, D., Paschal, K., Yao, C., Harris, J., "A Separation Control CFD Validation Test Case Part 2. Zero Efflux Oscillatory Blowing", AIAA-2005-0485 43rd AIAA Aerospace Sciences Meeting and Exhibit, Reno, NV 2005.

[9] Amitay M., Glezer, A., "Role of Actuation Frequency in Controlled Flow Reattachment Over a Stalled Airfoil" AIAA Journal Vol. 40, No. 2. February 2002, pp. 209 – 216.

[10] Glezer, A., Amitay, M., Honohan, A., "Aspects of Low- and High-frequency Actuation for Aerodynamic Flow Control" AIAA Journal Vol. 43, No. 7. July 2005, pp. 1501 – 1511.

[11] Wiltse, J. M., and Glezer, A., "Manipulation of Free Shear Flows Using Piezoelectric Actuators" Journal of Fluid Mechanics. Vol. 249, 1993, pp. 261-285.

[12] Hudy, L. M., "Simultaneous Wall-Pressure and Velocity Measurements in the Flow Field Downstream of an Axisymmetric Backward Facing Step", PhD. Dissertation, Michigan State University, 2005.

[13]Aditjandra, A., "Amplitude-modulated Excitation of a Separated Flow Using an Externally Driven Helmholtz Resonator" Masters Thesis, Michigan State University, 2006.

2 Experimental Setup

This chapter outlines the experimental setup and methods used in this investigation. Two main techniques were used to characterize the flow: single-hotwire velocity measurements, and static wall-pressure measurements. A detailed description of the setup, methods, and hardware is provided in the following sections.

2.1 Wind Tunnel and Facility

The experiment was conducted in the Flow Physics and Control Laboratory at Michigan State University, in a low-speed, wind tunnel. The tunnel is an open-return, low-turbulence-intensity, suction-driven facility. It measures approximately 9 meters long from end to end and its centerline is 1.35 meters above the floor. As seen in Figure 2.1, the tunnel consists of 6 sections: inlet, contraction, test section, pre-diffuser, diffuser, and fan sections.

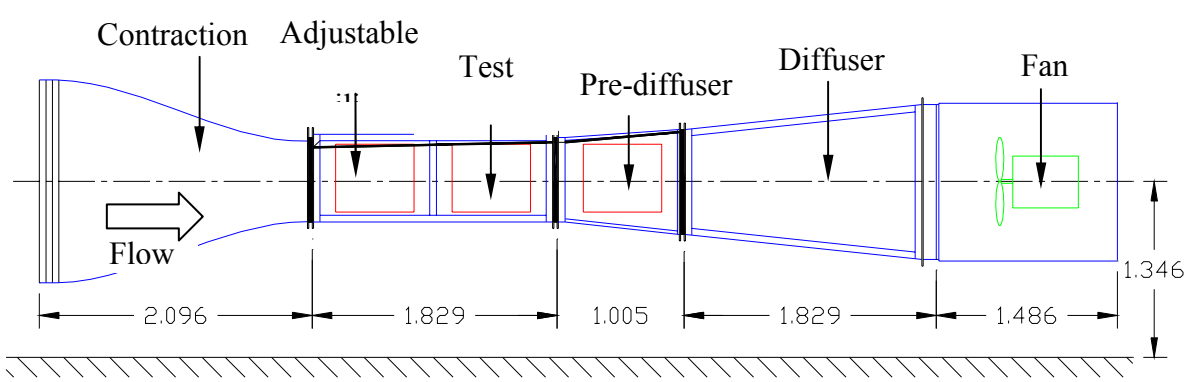

Figure 2.1 Schematic of wind tunnel (demission in meters)

The inlet consists of a square section of aluminum honeycomb with each side measuring

1.549 meters. The honeycomb is followed by three layers of high-porosity screens that reduce the turbulence intensity of the inlet air. Downstream of the screens, a contraction section is attached. The contraction is constructed from a laminate of fiberglass-reinforced, molded plastic and has an area contraction ratio of 6.25:1.

Immediately downstream of the contraction is the test section that is constructed from sealed plywood mounted in an aluminum frame. The test section is 1.83 meters long and has a square, cross section at the inlet, with each side measuring 610 mm. Four, hinged, acrylic windows, two on each side of the test section, allow access to the test model for inserting and positioning test devices and instruments. Additionally, the test section has an adjustable false ceiling that was set in order to establish a nominally zero-pressure-gradient condition along most of the length of the test section. The ceiling has 16.5 mm-wide slots running the length of the test section to allow introduction of instrumentation into the flow.

Adaptation of the test section's flow area to that of the driving fan is done through a combination of a pre-diffuser and diffuser. The pre-diffuser, which follows the test section, measures 1.005 m long and has a floor that diverges from the centerline by 6°. A movable ceiling in the pre-diffuser is adjusted to match the ceiling position at the end of the test section while providing smooth transition to the diffuser at the downstream end. The connection between the pre-diffuser and diffuser is not rigid. Instead the two units are aligned and separated by a layer of foam rubber; this is done in an attempt to eliminate the influence of any vibrations that are produced by the fan and motor on the test section. The diffuser is 1.83 meters long and has a divergence angle of 5.9°. It

serves to connect the pre-diffuser to the fan section, and recover the flow pressure. An adaptor between the diffuser and fan is used to transition from the square, cross-sectional area of the diffuser to the circular, cross section of the fan shroud. Finally, the fan section houses the motor and fan that draws air through the tunnel. The axial-flow fan is driven by a GE 15 HP DC motor that is controlled via an adjustable speed controller.

2.2 Axisymmetric Backward Facing Step Model

This investigation is conduced on an existing axisymmetric, backward-facing-step model. The model was designed, and the associated flow field around it was characterized by Hudy[1] and Li[2]. For excitation of the separated flow, the model was equipped with an externally-driven, Helmholtz resonator located at the point of separation that was developed and characterized by Aditjandra[3]. In the following, a brief description of the model and resonator is provided. For more detailed information the reader is referred to the aforementioned studies.

2.2.1 Model Dimensions

A schematic of the model can be seen in Figure 2.2. As labeled in the figure, the model is composed of several sections; which include the nose, 2D section, rotator section, Helmholtz resonator, step, support, and tail.

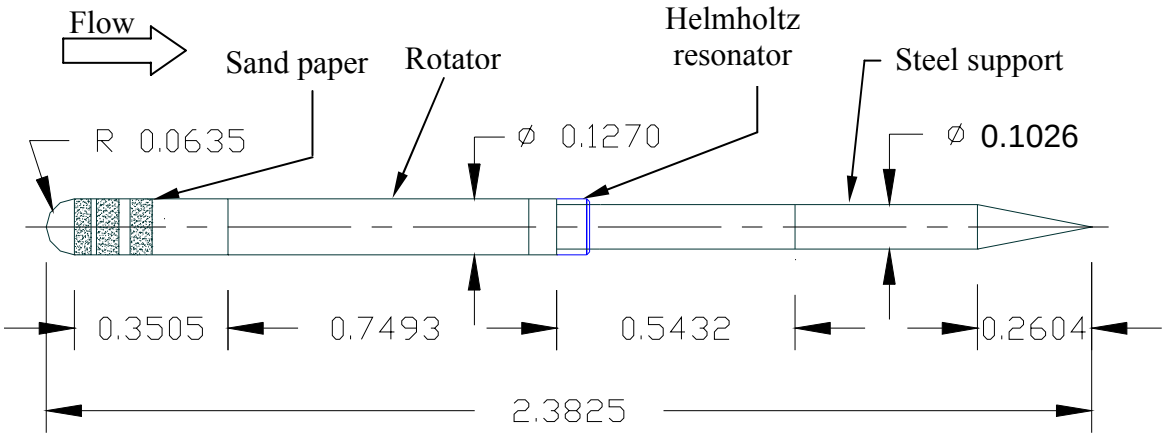

Figure 2.2 Schematic of the axisymmetric backward-facing-step model (dimensions in m)

The nose of the model is a hemisphere with a diameter of 127 mm. Following the nose is a segment created from a cylinder with an outer diameter of 127 mm that is 350.5 mm long. This section is intended for the initial development of a "two-dimensional" (i.e., azimuthally-uniform) boundary layer and is therefore referred to as the 2D section. Wrapped around the upstream end of the 2D section are three strips of 120-grit sandpaper that help to accelerate the development of the boundary layer towards a turbulent state. Downstream of the 2D section, a 749.3 mm-long cylinder of the same diameter as the 2D section composes the rotator section. This cylinder is capable of rotation about the centerline of the model in order to produce a three-dimensional boundary layer at separation; however, in the present experiments, this capability was not utilized.

Just downstream of the rotator section, there is a hollow cavity that acts as an externally driven, Helmholtz resonator. This resonator, which is described further in 2.2.3, is the mechanism that was used to force the flow at the point of separation. At the downstream end of the resonator, the back step is created by an abrupt decrease in the outer diameter of the resonator to 102.6 mm, producing a step of 12.2 mm. The region downstream

of the step is the separation/reattachment flow region, which is the main focus of the present investigation. Beneath this flow region, the top surface of the model is fitted with a removable insert containing 32 pressure taps and 32 microphones, side by side, that may be used for mean- and unsteady-pressure data acquisition respectively. Farther downstream of the reattachment region, resides the model support module; which, with the assistance of four 1mm-diameter piano wires at the upstream end of the model, holds the model firmly in place and allows for adjustment to align the model parallel to the freestream. The last model component is the tail, which is a 260 mm-long cone that is used to reduce the strength of any separation at the end of the model. For more detailed specifications of the model construction, see Hudy[1].

2.2.2 Measurement Region

The data-acquisition region downstream of the step contains four primary measurement locations in a plane perpendicular to the mean flow that are denoted as north, east, south, and west, as seen in Figure 2.3

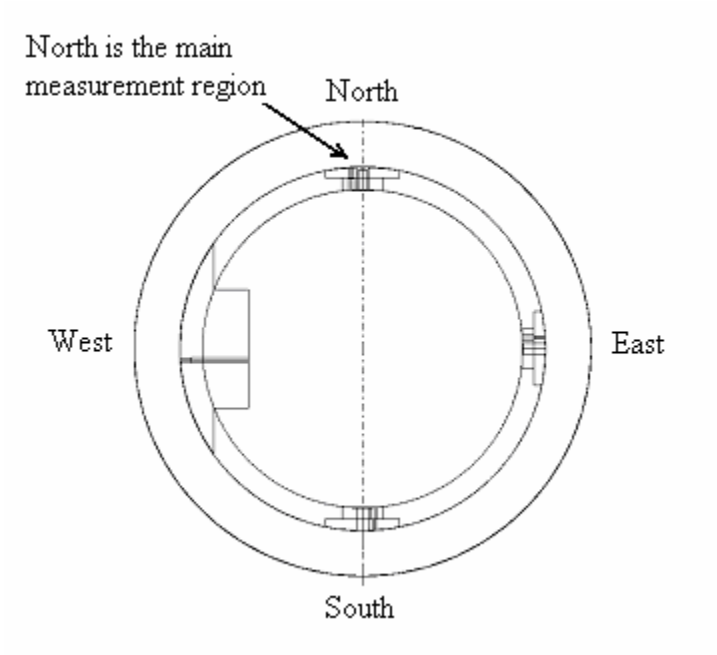

Figure 2.3 Cross section of the measurement region downstream of the back step (flow is out of the paper)

The majority of the measurements were conducted on top of the model (north side) because at this location the model contains a wall-sensor insert (or I-plate) with 32 static pressure taps that were used to obtain details of the mean-pressure distribution beneath the separation bubble under forced and unforced conditions. Furthermore, the studies of Hudy[1] and Aditjandra[3] were both conducted at this location. To stay consistent with these studies, particularly the latter, which is directly related to this one, the north position was selected for the present measurements. The east, south, and west locations contain additional wall inserts fitted with static-pressure taps (8 at each location) that are used for model alignment.

The static pressure taps are offset 1mm from the center of the I-plate and are spaced at 4.76 mm center to center. It is important to note that the streamwise location of the taps

was selected for earlier studies not employing a flow excitation device. Subsequent assembly of the resonator on the model resulted in covering the five upstream most pressure taps. Thus, the first usable pressure tap immediately downstream of the step is the 6th tap, which is located 11.7 mm downstream of the separation point. This reduced the number of taps used in the acquisition to 18. The resulting streamwise range for the mean-pressure data extended from 0.96 to 7.99 step heights with inter-sensor spacing of 0.39 step heights.

2.2.3 Resonator

For this investigation, the unsteady disturbance that "controls" the flow was generated by an externally driven, Helmholtz resonator located at the point of separation. The resonator was composed of three pieces: the outer shell, the shell supports, and the end cap. A cross-section drawing of the resonator and step region can be seen in Figure 2.4

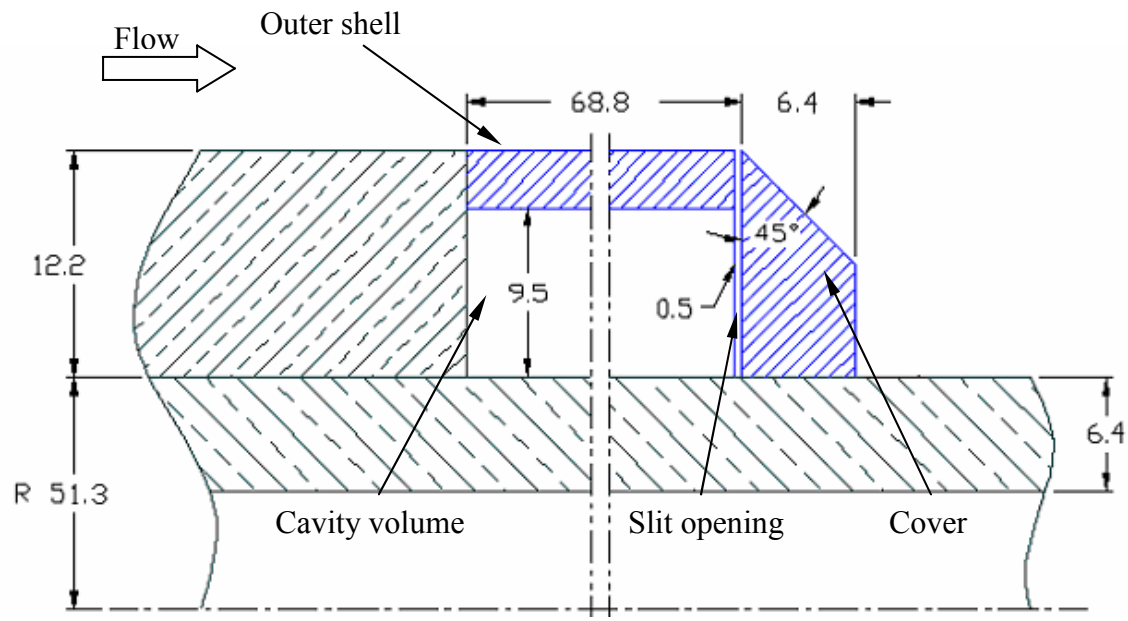

Figure 2.4. Cross section drawing of the resonator and step region (note drawing is not to scale; dimensions in mm)

The outer shell is made of a ring of acrylic that has a 127 mm outer diameter; a 117.5 mm, inner diameter; and is 68.8 mm long. The outer shell is supported by four small brackets (see Figure 2.5). These supports are necessary to maintain proper positioning of the outer shell. The end cap is a machined ring of acrylic that is placed just downstream of the outer shell to create a 0.5 mm gap forming the neck, or slit, of the Helmholtz resonator. The end cap has a tapered tip that allows the disturbance to be generated as close to the point of separation as possible while still retaining structural integrity of the end cap. When assembled, the resonator has an internal volume of 219.762 cm^3 and the resonant frequency was determined by Aditjandra to be 657 Hz.

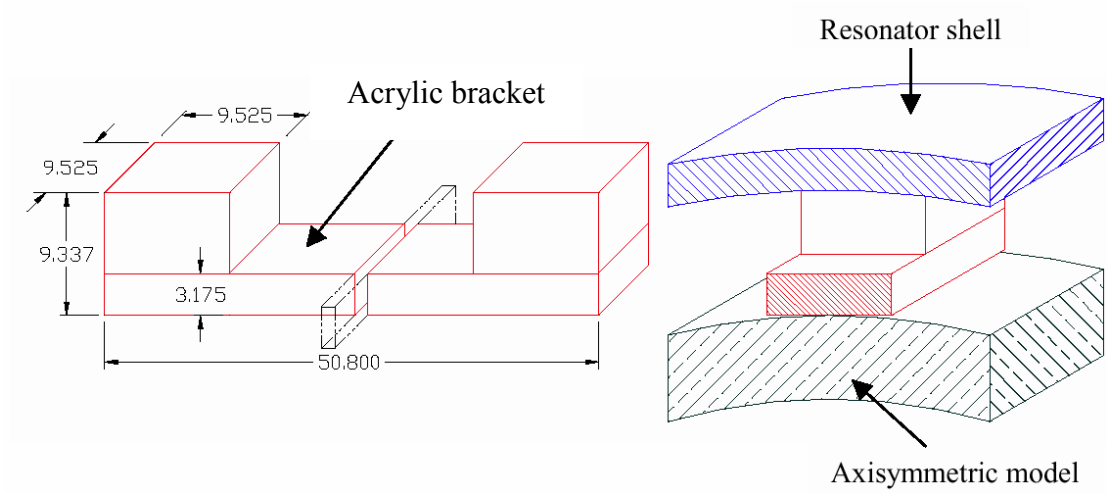

Figure 2.5 Geometry of the resonator's outer shell supports (dimensions in mm)

2.2.4 Forcing System

The resonator is externally driven by a speaker that is located upstream of the wind tunnel, as seen in Figure 2.6. The speaker used was a 0.385 m-diameter, 450-Watts Eminence LLC subwoofer (model Kappa 15) that was located on the centerline of the

tunnel, approximately 2.3 meters upstream of the entrance of the wind tunnel.

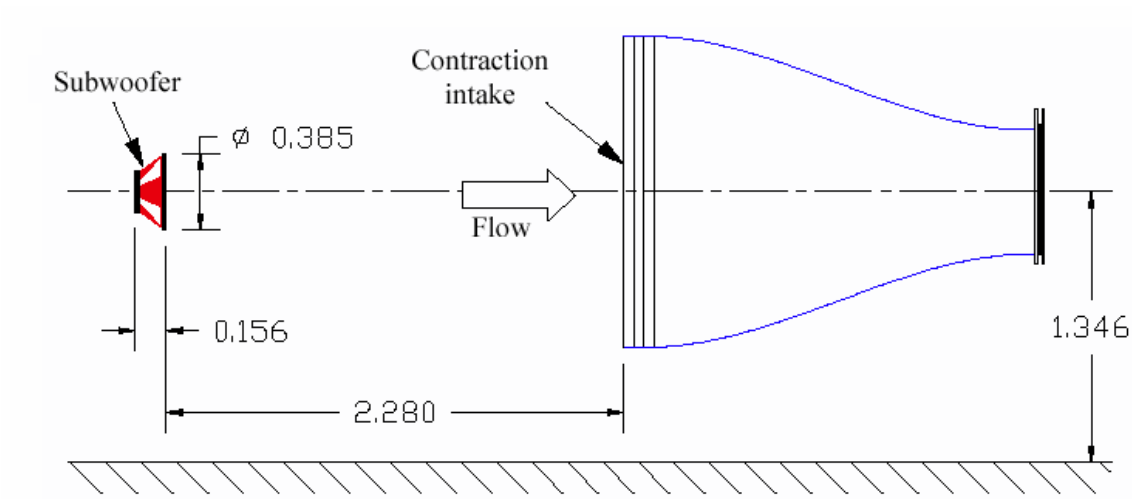

Figure 2.6 Location of the speaker used to drive the resonator relative to the wind tunnel (dimensions in meters)

The speaker was powered by a two-channel, Hafler (Transana P 1000), power amplifier. The amplifier was used in strapped single-channel mode to boost the output power from 110 to 220 watts. The input signal to the amplifier was generated from two Hewlett Packard (model 33120A) function generators (model 33120A).

As known from the literature (e.g., Greenblatt and Wygnanski[4]), a separated flow responds best to periodic excitation at an optimum non-dimensional, forcing frequency (normalized with the freestream velocity and a length-scale characteristic of the streamwise size of the separation bubble) on the order of 1; i.e., $O(1)$. Therefore, for effective forcing of the flow, the resonator's should have a non-dimensional, resonant frequency of $O(1)$ as well. However, one issue that arises when forcing the flow directly at the optimum forcing frequency is that the forcing system would produce acoustic noise (originating from the speaker in the current study) at the same frequency as that of the

forced flow structures. This acoustic noise would be difficult to separate from the wall-pressure fluctuations produced by the forced flow structures when using surface-mounted microphones to investigate the wall-pressure characteristics beneath the forced flow. Although such wall-pressure measurements are not the concern of this study, they are part of the overall research goal of studying the axisymmetric, back-step flow under natural and force flow conditions, which has been studied by Li[2], Hudy[1], and Aditjandra[3]. In fact, the latter study developed the driven-resonator device with the specific objective of producing periodic excitation of the separation bubble without contaminating wall-pressure sensors by sound resulting from the actuation device.

To eliminate the aforementioned problem as well as to generate a forcing effect at frequencies substantially below the resonant frequency of the resonator, amplitude-modulated excitation was employed through multiplication of two sine waves as given in equation (2.1).

$$F(t) = A_m \sin(2\pi f_m t)\sin(2\pi f_c t) \tag{2.1}$$

where F(t) is the amplitude-modulated signal, A_m is the amplitude of the signal, f_m is the modulation (low) frequency, and f_c is the carrier (high) frequency. When forcing the flow, f_c was set equal to the resonant frequency of the resonator and f_m was set to half the frequency at which the flow is to be excited. This method proved effective in exciting the flow at $2f_m$ because of the non-linearity of the Helmholtz resonator when driven by high-intensity sound. For further explanation of the coupling mechanism the reader is referred to Aditjandra[3].

Although, it is possible to generate an amplitude-modulated forcing signal from a single function generator, this proved to be problematic in the present work. To clarify, it is helpful to recall that the amplitude-modulated signal given by equation (2.1) consists of the sum of two *equal*-amplitude sinusoidal signals with frequencies of f_c-f_m and f_c+f_m. Thus, when using a single function generator to drive the speaker, one feeds two, equal-amplitude, acoustic sine waves at these two frequencies into the wind tunnel. However, due to acoustic resonance of the wind tunnel, and acoustic wave reflections produced by components downstream of the test section, (i.e., fan, motor, walls etc.), standing wave patterns are established along the test section. The relative strength of these patterns is generally a function of frequency and they cause the sound amplitude of each of the two waves to change at different streamwise locations within the tunnel. Therefore, at the location where the resonator's "neck" exists, the sound amplitude at f_c-f_m and f_c+f_m was found to become different, and the modulation quality was generally poor. More specifically, referring to Figure 2.7, the modulation quality may be quantified using a "modulation index" (MI), defined as

$$MI = \frac{m}{A_{me}} \tag{2.2}$$

where A_{me} is the peak of the modulation envelope and m is as defined in Figure 2.7. To maximize the amplitude of the disturbance induced in the flow at $2f_m$, an MI of 1 is desired. With the use of a single function generator it was not possible to guarantee that this is the case for all choices of f_m, as describe above.

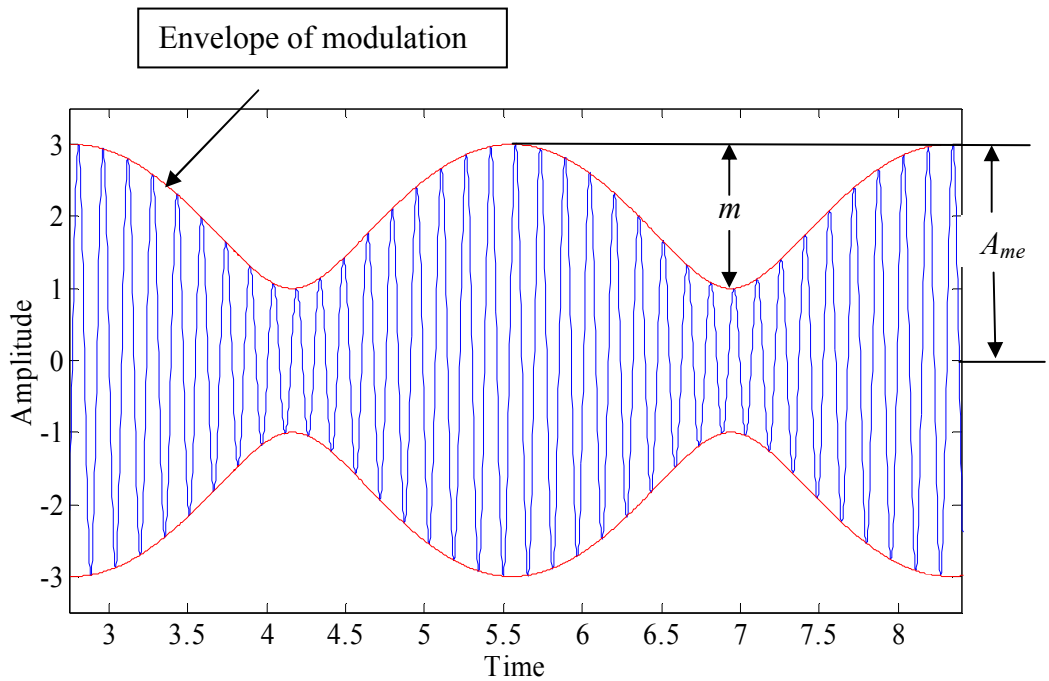

Figure 2.7 Example of an amplitude-modulated sine wave with MI = 2/3

To counteract the poor modulation effects, the amplitude modulation signal was generated utilizing two function generators. In particular, one of the function generators was used to provide a sine wave at frequency of f_c+f_m, while the other generator produced a second wave at frequency of f_c-f_m. This allowed independent control of the amplitude of each wave, to produce a signal of the form

$$F(t) = A_1 \cos(2\pi(f_c - f_m)t) + A_2 \cos(2\pi(f_c + f_m)t) \tag{2.3}$$

A_1 and A_2 were then adjusted independently to produce an acoustic signal with MI = 1 *at* the neck of the resonator. The procedure to reach this condition is outlined later in 2.4.2

2.3 Data Acquisition Systems

For this investigation, different types of information are recorded. These are mean

static pressure on the surface of the model, freestream velocity, air temperature, flow velocity downstream of the step, speaker forcing signal, hotwire position, and images for probe positioning. In order to acquire this information, two independent data acquisition systems controlled by a number of custom LabView software programs were utilized. The primary system was an analog-to-digital (A/D) converter employed for acquisition of the velocity, pressure, temperature, and forcing signal data. A PC-based National Instrument A/D board (model NI 6024 E) with 16 single-ended, analog-input channels and a maximum sampling rate of 200,000 Hz at 12 bit resolution was used to capture these five signals. This board has an adjustable input-voltage range for each channel; by using the smallest possible range that still captures the entire signal, the voltage resolution for each signal can be maximized. The available voltage ranges for the board are: ±10 V, ±5 V, ±0.5 V, and ±0.05 V that correspond to resolutions of 4880 μV/div, 2440 μV/div, 244 μV/div, and 24 μV/div respectively. Due to the channels being sampled sequentially there is an inter-channel time delay of 5 μs. This time delay, when accumulated over all five channels, is equal to 0.09% of the period of one forcing cycle.

The second system was used for acquiring images for hotwire positioning. To this end, an NI-IMAQ PCI -1411 single-channel, image-acquisition board (frame grabber) was used to capture the output of a standard-video CCD camera that is described later in 2.3.5. The IMAQ card is capable of acquiring both black and white and color RS-170, CCIR, NTSC, and PAL standard video images; RS-170 mode is utilized in this investigation.

2.3.1 Mean Static Pressure

Meanstatic-pressure data were sampled in the region downstream of the step via static-pressure taps embedded in the surface of the model's I-plate, as described previously. These pressure taps are connected to a 48-port Scanivalve Corporation (48D9-1/2) pressure scanner using long urethane tubing. The scanner was driven by a rotary solenoid (48D9M-1/2), which was controlled by a homemade circuit. The latter is designed to step the scanner from one port to the next either manually by depressing a button, or through a connection to one of two digital to analog channels of the NI 6024 E board described above.

The output of the Scanivalve was connected to the negative port of a Setra model 239 pressure transducer with a range of 0 -125 Pa and a sensitivity of 0.04 V/Pa. The positive port of the Setra was connected to the static-pressure port of a pitot tube placed a short distance upstream of the step to provide a reference pressure for the measurements. The static pressure taps at which data were acquired covered a streamwise distance extending from x/h = 0.96 to x/h = 7.99 in increments of 0.39 step heights. The output of the Setra transducer was connected to the data acquisition system with the input range set to ± 0.5V.

2.3.2 Pitot Tube

The pitot tube in this experiment has two purposes: to measure the freestream velocity and to provide a reference, freestream, static pressure for the surface mean-pressure measurements. An 8 mm-diameter, pitot tube was placed in the freestream through a slot in the ceiling of the test section. The tube was located 0.55 meters upstream of the step and 63.5 mm below the ceiling of the test section. With a ceiling's boundary layer

thickness of approximately 38 mm at this location, the tube was in the freestream. The total and static pressure ports of the pitot tube were connected to opposite ports of a 0-1torr Baratron (model 223BD) pressure transducer using urethane tubing. The transducer outputs a 0-1V signal that was connected to the data acquisition system with the input range set to ± 0.5V.

2.3.3 Temperature

Temperature data were needed to calculate the density of air for pitot-tube velocity measurements, and were also employed for hotwire-velocity-measurement correction. An Omega (DP-25-TH) thermistor was used to measure the temperature of the freestream fluid downstream of the model. The thermistor used has an analog output signal with a sensitivity of 0.1V per °C and a range of 0-50 °C. The output of the thermistor was connected to the data acquisition system with the input range set to ± 5V.

2.3.4 Hotwire Velocity

A single, hotwire probe was used to measure the velocity in the investigated flow. The single wire can measure the velocity magnitude, but it is incapable of measuring the velocity direction. Therefore, it cannot resolve the measurement into different components. In comparison, an x-wire probe may be used to obtain two components of the velocity. However, the x-wire could introduce spatial averaging errors that are particularly significant for measurements immediately downstream of the step where the shear layer is very thin. Therefore, for this first study of the velocity field of the forced flow it was decided not to employ an x probe.

The hotwire used in this investigation was constructed from 3.75 μm-diameter tungsten wire with 0.97 mm sensing length, yielding a cold resistance of 6.4 ohms. The hotwire was controlled with a TSI, Flowpoint, constant temperature anemometer (CTA) with the overheat ratio set to 1.7. The hotwire was attached to a dual-axis traversing mechanism as seen in Figure 2.8.

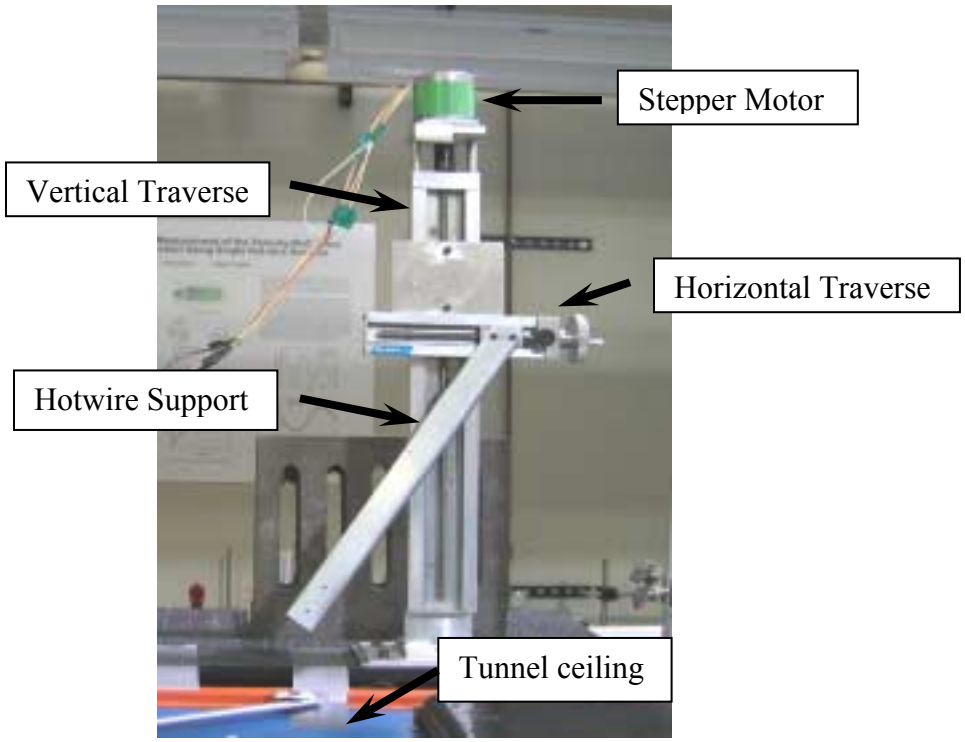

Figure 2.8 Picture of Hotwire Traverse System

The vertical traversing unit was a 15" Velmex A25 series unislide screw drive traversing unit with a pitch of 40 turns per inch of travel. It is driven by a TMG Model 5618S-01 hybrid stepper motor that has an angular resolution of 800 steps per revolution, which provides 0.823 μm of vertical motion per step when calibrated. The stepper motor is computer controlled using a custom-developed LabView program that controls the stepper motor's power/controller box. Orthogonally mounted to the vertical traverse

carriage is a 6" Velmex A15 series unislide screw drive traversing unit to allow streamwise translation of the hotwire probe. The horizontal traversing unit has a lead screw with 40-turns-per-inch pitch and is turned manually using a knob that is graduated at increments of 0.01mm. The traversing accuracy of the unit is specified by the manufacturer to be within 0.033 mm per 20 cm of travel.

The hotwire is mounted to the end of a long of 6 mm by 12 mm steel support rod that is connected to the horizontal traversing unit's carriage via an aluminum support bar (see Figure 2.8) and fed through the slot in the ceiling of the test section. The steel support rod is covered by an aluminum airfoil tubing to reduce drag. The entire traversing assembly is mounted on a large aluminum plate positioned on top of the test section and is supported by vibration isolation material.

For this investigation the constant temperature anemometer output falls in the range of 1-2 Volts. To capture the hotwire signal, an A/D input range of ± 5V was used. However, to optimize the digitization resolution of the fluctuating component of the signal, the hotwire output was also routed through a Larson-Davis preamplifier/power supply (model 2200c) that functioned as a high-pass filter with a cut off frequency of 1.6 Hz and 20db (i.e., factor of 10) gain. This generated an amplified mean-removed signal that was recorded at higher resolution than the full signal by utilizing ± 0.5V A/D input range. During post-processing of data, the mean-removed signal was added to the mean voltage from the full hotwire signal to recover the full signal with a more accurately captured fluctuating component.

2.3.5 Positioning Camera System

A camera system mounted outside the test section was utilized for positioning the hotwire above the surface of the model. The camera used for this operation was a standard video Sony (model XC-75) Charge Couple Device (CCD) camera. The camera was connected to a National Instruments IMAQ board model PCI-1411 frame grabber. For positioning the hotwire, the camera was fitted with a Nikkor 500 mm (model NH - 27) lens. The area where the probe was to be positioned was illuminated with a high-intensity, florescent light from Stocker & Yale, Inc. (model 13 Plus Lite Mite Series). A sample of the hotwire-positioning images can be seen in Figure 2.9.

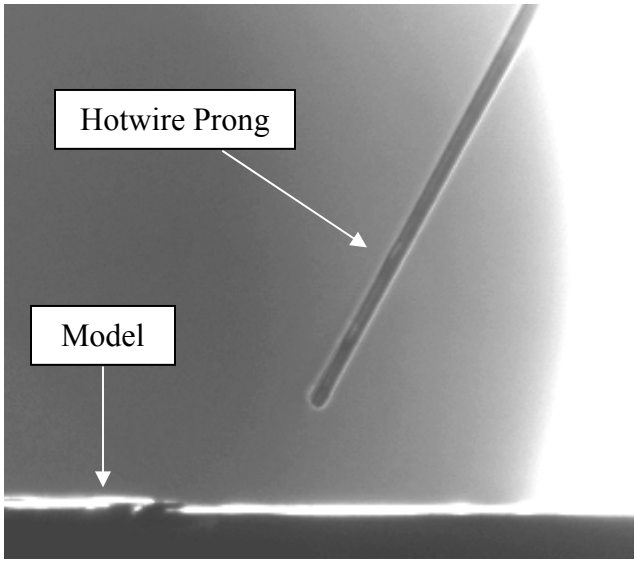

Figure 2.9 Sample image of the hotwire above model wall during positioning procedure

2.4 Experimental Procedure

This subsection gives a summary of the experimental procedure and methodology that

was used in the collection of data.

2.4.1 Testing Parameters

Two different sets of data acquisition parameters were used: one set for the velocity data and the other for the mean-pressure profiles. For the velocity data, the acquisition rate was set to 8000 Hz, acquiring a total of 2^{18} (262,144) samples. This sampling rate was determined to be sufficiently above twice the highest-frequency velocity fluctuations produced by the flow structures (approximately 1 kHz for the current flow), therefore eliminating the possibility for aliasing. The duration was selected to be long enough to capture multiple cycles of the velocity produced by the lowest-frequency structures. More specifically, with this selection of data sampling parameters, frequency spectra could be obtained with a resolution of 4 Hz and random uncertainty of 8.8%.

The second set of testing parameters, which were used to sample the mean surface-pressure, corresponded to a sampling rate of 1500 Hz and15,000 numbers of samples. These parameters produced a 10-second duration for the acquired time series, which was determined to be sufficient to accurately calculate the average pressure. The rationale for this determination will be further discussed in 2.4.3.

2.4.2 Forcing-Signal Parameters

As explained earlier, the flow forcing in this investigation was achieved by externally driving a Helmholtz resonator with a speaker located upstream of the wind tunnel entrance. The carrier frequency of the forcing signal was set to a nominal frequency of 630 Hz, which was slightly different from the resonator's resonance frequency of 657 Hz.

This was done to obtain the strongest possible fluidic disturbance by the resonator for a given driving-sound level. As explained by Aditjandra[3], the shift in the frequency of the strongest disturbance from the resonator's resonance frequency is caused by wind tunnel's resonance.

The carrier frequency value of 630 Hz was fine tuned from day to day within a few Hz due to the effect of changes in the ambient temperature on the speed of sound (and hence on the resonance frequency of both the forcing device and wind tunnel). To account for these temperature variations in the resonance frequency, the carrier frequency was always determined empirically prior to data acquisition on different days. The procedure involved utilization of a hotwire that was placed 0.02 mm above the resonator's slot while the speaker was driven by a sine wave produced from a single function generator. A sketch of the hotwire location relative to the resonator can be seen in Figure 2.10. The output of the hotwire was displayed on an oscilloscope and the frequency of the input sine wave was adjusted within a few Hz around 630 Hz until the fluctuation of the hotwire trace reached a maximum. The frequency setting of the function generator at this condition was then used as the carrier frequency in equation (2.3).

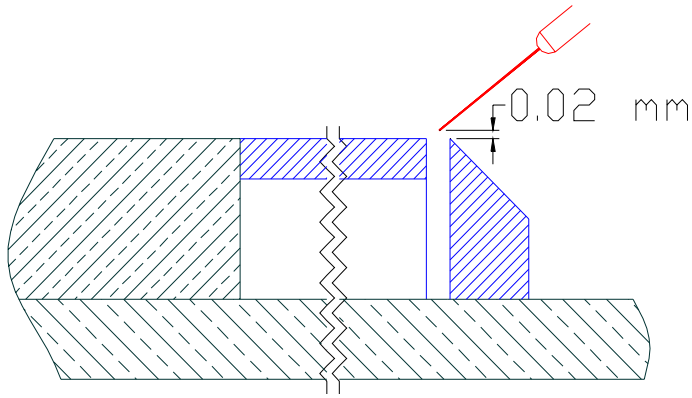

Figure 2.10 Location of hotwire for carrier frequency determination

After the determination of the carrier frequency, it was also important to set the values of A_1 and A_2 to achieve a modulation index of 1, as discussed in section 2.2.4. Two function generators were used to create the frequencies required by equation 2.3: (f_c+f_m) and (f_c-f_m). The signals were combined using a homemade, operational-amplifier, summation circuit, the output of which was routed to the amplifier that drives the speaker. The resulting velocity of the jet at the exist of the resonator's slot was monitored using the hotwire signal, which was observed on the oscilloscope while the amplitude of each function generator is adjusted independently until the modulation index is determined visually to be 1.

Figure 2.11 is a hotwire trace of the jet velocity showing what is considered to be good modulation. As seen from the figure, the amplitude of high-frequency sinusoidal oscillations (at the carrier frequency) is made to modulate in time. The modulation corresponds to an MI of 1 since the oscillations are completely turned off when the amplitude is minimum (for example, when the jet velocity approaches zero at t = 0.015s in Figure 2.11). It is noted here that the rectified-wave appearance of the trace in Figure

2.11 is due to the existence of a streaming flow component of the jet velocity (see Aditjandra) and rectification effects due to direction insensitivity of the hotwire. For the velocity data presented in this document, the modulation settings used may be seen in Table 2.1. Note that these values correspond to f_c = 632 Hz and f_m = 18 Hz, where the selection of f_m is described in the following paragraph.

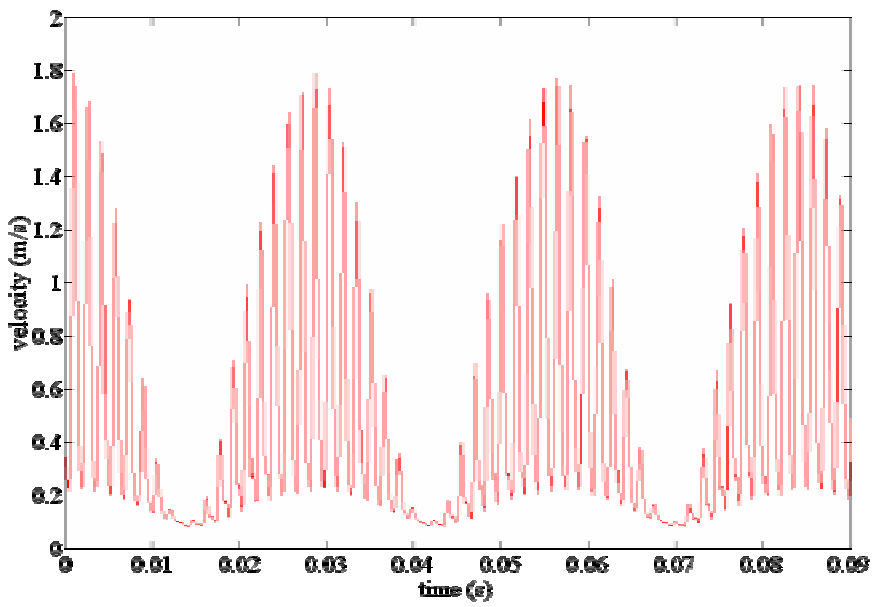

Figure 2.11 Amplitude modulated resonator's jet velocity

Table 2.1 Function generator settings for the forcing signal

	Function Generator 1	Function Generator 2
Amplitude	1020 mV	980 mV
Frequency	650 Hz	614 Hz

The amplitude-modulated signal produces an unsteady jet that grows and decays at a rate of twice the modulation frequency. This may be seen from the hotwire trace of the velocity of the jet shown in Figure 2.12. The red trace shown in the figure is corresponds to one full cycle of the modulation frequency. When this trace is low-pass filtered to obtain the low-frequency disturbance that actually excites the flow, it is evident that the frequency of the filtered signal (shown using black line in Figure 2.12) is twice as high as the modulation frequency. Note that the amplitude and frequency ($2f_m$) of the low-pass filtered signal is what is employed here to obtain the non-dimensional, forcing amplitude and frequency values.

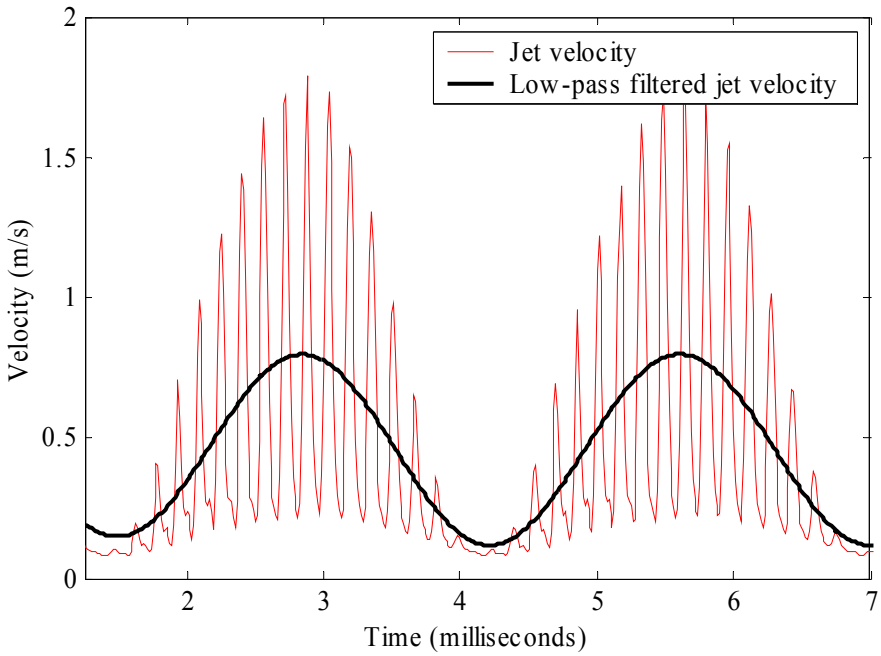

Figure 2.12 Hotwire trace of the flow velocity above the resonator's slit

A non-dimensional forcing frequency of $F^+ = 0.6$ was determined to be the optimal

forcing frequency from the investigation by Aditjandra[3], where

$$F^{+} = \frac{2 f_m x_r}{U_\infty} \tag{2.4}$$

with x_r being the mean reattachment length. As discussed by, for example, Greenblatt and Wygnanski[4], F^+ is the proper non-dimensional forcing frequency to use for unsteady separation control. The length scale used in normalizing the frequency should be descriptive of the size of the separation bubble in the streamwise direction. For the back-step flow, the mean reattachment length is typically used.

Finally, the forcing level was also selected based on the study of Aditjandra[3] who found that increasing the forcing amplitude of the resonator within the limits of the audio amplifier results in a larger effect on the flow. Therefore, to study the forced flow with the biggest modification relative to the natural case, it was desirable to force the flow at the largest amplitude attainable by the flow excitation system. However, to maintain the same forcing level from day to day, one needs the ability to fine tune the amplifier gain to offset the small fluctuation in resonator response caused by changes in the ambient temperature (as discussed earlier). Hence, an amplitude lower than the maximum allowed by the system was used to allow for this correction. The non-dimensional, forcing level used for this investigation was $C_\mu = 0.0434\%$, where

$$C_\mu = \frac{2 d u_{j,rms}^2}{h U_\infty^2} \tag{2.5}$$

d is the slot width, h is the step height, and $u_{j,rms}$ is the rms velocity measured

immediately above the resonator's exit. It is important to note that $u_{j,rms}$ is calculated based on the sinusoidal component of u_j at the forcing frequency of the flow; i.e., $2f_m$. This is done by low-pass filtering the hotwire signal to remove the signal components at f_m+f_c and f_m-f_c before calculating the rms as seen in Figure 2.12.

2.4.3 Mean-Pressure Profiles

Mean-pressure profiles were measured in the separating/reattaching flow region downstream of reattachment to quantitatively examine the extent to which the forcing system was affecting the flow. The information was obtained from the static-pressure taps located downstream of the separation point as described in section 2.3.1. Data acquisition settings were determined based on the study of Hudy[5]. Tests conducted by Hudy[5] showed that 10 seconds of data is the minimum average duration required to calculate the mean pressure with acceptable accuracy. Moreover, the system requires at least one second to stabilize after switching ports on the Scanivalve before data sampling can begin.

Figure 2.13 shows the mean-pressure coefficient (C_p) plotted vs. downstream position normalized by step height, where

$$C_p = \frac{P_s - P_r}{\frac{1}{2}\rho U_\infty^2} \tag{2.6}$$

P_S is the mean surface pressure at a given x location, P_r is the reference pressure from the pitot tube (see section 2.3.2), ρ is the air density, and U_∞ is the freestream velocity.

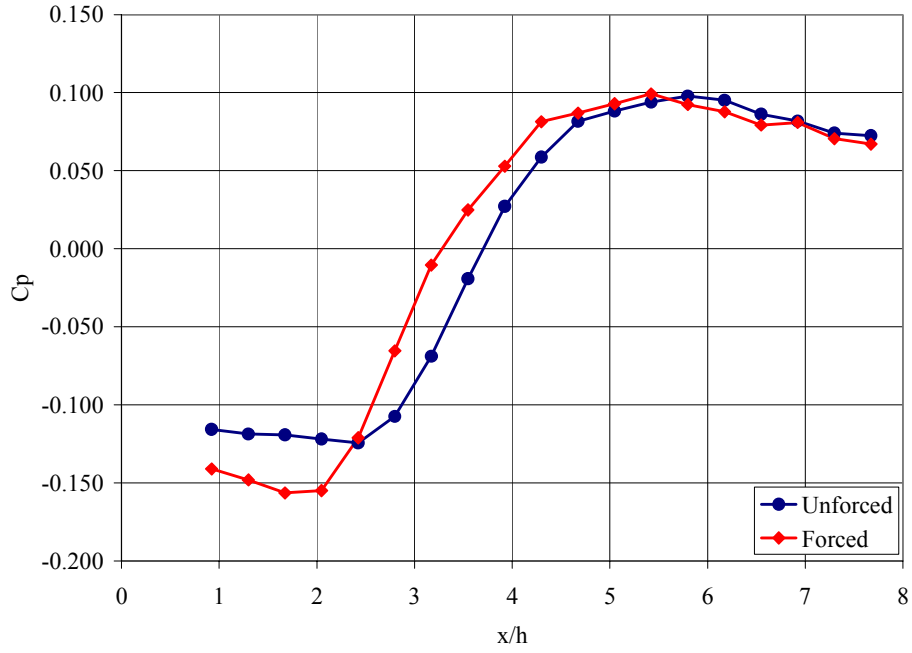

Figure 2.13 Forced- and unforced-flow mean-pressure profiles downstream of the step

The curve corresponding to the unforced-flow case in Figure 2.13 is consistent with a typical, backward-facing-step, wall-pressure profile. The profile clearly shows the broad negative Cp peak associated with the low-pressure recirculation bubble in the region of $0 \leq x/h \leq 2.5$. Farther downstream, there is a pressure recovery region that extends to approximately $x/h = 5$. For $x/h > 5$, the flow is completely reattached and the pressure gradually approaches the freestream, static pressure.

The forced-flow, wall-pressure distribution exhibits the same general characteristics, however there are important differences. The negative Cp peak associated with the recirculation bubble has a lower negative pressure coefficient, and the extent of this peak does not extend as far downstream as under the unforced condition. This suggests that the average recirculation flow is stronger and it occupies a smaller space. Additionally,

the pressure recovery begins farther upstream, at approximately x/h = 2, relative to the unforced case. All of these features are consistent with data seen in the literature for periodically-excited separation bubbles; e.g., Greenblatt *et.al*[6].

2.4.4 Velocity Acquisition Procedure

This section outlines the testing procedures and methodology for acquiring the hotwire velocity profiles at various locations within the measurement domain of interest.

2.4.4.1 Hotwire Calibration

Hotwire calibration was needed for two purposes: first, to obtain the required constants to relate the voltage output form the CTA to the velocity and second, to ensure that this relationship between voltage and velocity does not drift during testing. The voltage to velocity relationship used here is that suggested by Collis and Williams[7]

$$E^2 = A + Bq^{0.45} \tag{2.7}$$

where A and B are empirical constants obtained though calibration, E is the voltage output form the CTA, and q is the velocity magnitude. A and B are obtained by placing both the hotwire and a pitot tube in the freestream inside the test section and exposing them both to the same velocity. By acquiring E and q data for a range of different freestream velocities, a least-squares curve fit to equation (2.7) provides the constants A and B.

Typical calibration data and associated curve fits are shown in Figure 2.14.

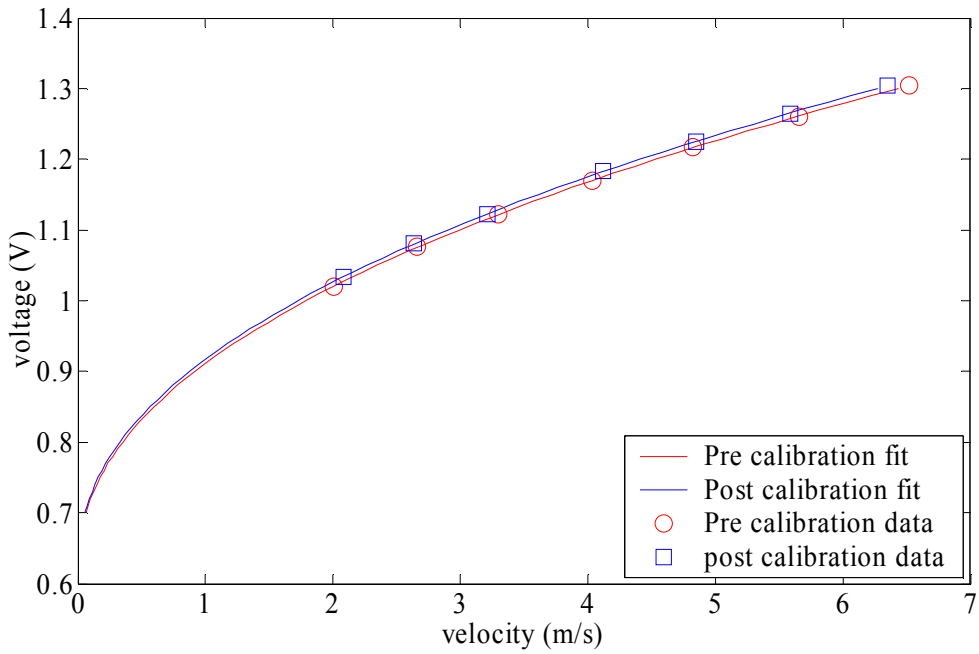

Figure 2.14 Sample Hotwire calibration curves

The maximum deviation of the data from the calibration curve is less than 1%. Furthermore, very little change is found between the calibrations obtained pre and post the experiment. More specifically, the maximum pre- to post-calibration difference is less than 1.5%.

2.4.4.2 Velocity Measuring Positions

In order to study the velocity field, single-hotwire measurements were conducted at several locations downstream of the separation point. Three main parameters were taken into account when deciding on these locations. x resolution, y resolution, and the flow region within which strong reverse flow from the recirculation bubble would make it difficult to interpret the single-wire measurements. Based on examination of PIV data taken by Hudy[1] on the same test model, a region with significant probability of upstream

velocity was identified from the forward flow probability seen in Figure 2.15 and excluded from the present, measurement domain. The hotwire sampling points (shown using black dots in Figure 2.15) that encroach to low, forward-flow-probability areas were deemed necessary to avoid missing relevant data under the forced-flow condition, where the recirculation bubble shrinks.

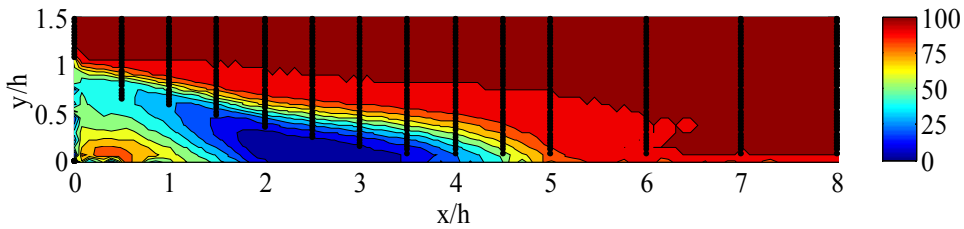

Figure 2.15 Forward flow probability from PIV measurements of Hudy (color map); and hotwire measurement locations for the present investigation (black dots)

Data were taken at every half-step height downstream of the step from $0 \leq x/h \leq 5$ and every step height from $5 < x/h \leq 8$. This covers a range that is approximately twice the mean reattachment distance ($x_r/h \approx 4$) for the unforced case. This x_r value is an approximate estimate given by Aditjandra[3] from surface-pressure measurements.

Data were taken in the y direction at increments of 0.4 mm starting from 1 mm above the surface of the model downstream of the step up to 1.5 step heights, excluding the region determined to be in high-reverse-flow areas. This resulted in approximately 10 y measurement locations within the thin shear layer downstream of separation. The black dots in Figure 2.15 show the full measurement grid, which consists of 14 different x locations and a total of 513 grid points.

2.4.4.3 Testing Procedure

The process to acquire the hotwire velocity information was automated through the use of a LabView program that was designed to capture velocity data at a number of y locations for a given x position. First, the probe was positioned at the desired x/h location and the lowest y/h position. This was done with the assistance of the CCD camera described in 2.3.5. However, the CCD camera needed to be calibrated to determine the imaging scale; i.e., distance in the object plane per pixel in the image plane.

The imaging scale was determined by positioning the hotwire probe at an arbitrary distance above the model, but within the view of the camera, and acquiring an image. Following this, the probe was moved vertically a known distance by the stepper motor, which was further verified by a dial indicator with an accuracy of 0.0127 mm. A second image was then acquired, and the number of pixels per mm could be calculated by locating the pixel location of the probe tip in the first and second image and dividing the difference between these pixels by the probe translation distance. This procedure was repeated 5 times to obtain an average and reduce random errors that may be present such as that associated with accuracy of locating the probe tip. A typical imaging scale factor was 52 μm/pixel.

After the hotwire was calibrated and properly positioned, the wind tunnel was set to operate at a freestream velocity of 3.25 m/s via the adjustable speed controller of the fan's motor which corresponds to a Reynolds number based on step height of R_{eh} = 2,630. As described in section 2.3, the hotwire voltage, high-passed-filtered and amplified hotwire voltage, forcing signal, freestream velocity and temperature were all

sampled simultaneously. During post processing, the temperature measurements were used to correct the hotwire output for any temperature change between the calibration and main experiments. Additionally, any freestream velocity fluctuations (which were limited to less than 2.5%) were taken into account when normalizing the long-time and conditional statistics presented in later chapters. It is to be noted that the selected velocity of 3.25 m/s is the lowest stable velocity that can be established in the tunnel. This selection of such a low speed was motivated b the desire to maximize the non-dimensional strength of the flow control.

2.5 References

[1] Hudy, L. M., "Simultaneous Wall-Pressure and Velocity Measurements in the Flow Field Downstream of an Axisymmetric Backward Facing Step", PhD. Dissertation, Michigan State University, 2005.

[2] Li, Y. and Naguib, A.M., "High-Frequency Oscillating-Hot-Wire Sensor for near- Wall Diagnostics in Separated Flows," American Institute of Aeronautics and Astronautics Aerospace Journal, Vol. 43, No. 3, 2005, pp. 520.

[3] Aditjandra, A., "Amplitude-modulated Excitation of a Separated Flow Using an Externally Driven Helmholtz Resonator" Masters Thesis, Michigan State University, 2006.

[4] Greenblatt, D and Wignanski, I., "Control of Separation by Periodic Excitation", Progress in Aerospace Sciences, Vol. 37, Issue 7, 2000, pp. 487 - 545.

[5] Hudy, L. M., "Simultaneous Wall-Pressure Array and PIV Measurements in a Separating/Reattaching Flow Region", M.S. Thesis Michigan State University 2001.

[6] Greenblatt, D., Paschal, K., Yao, C., Harris, J., "A Separation Control CFD Validation Test Case Part 2. Zero Efflux Oscillatory Blowing", AIAA-2005-0485 43rd AIAA Aerospace Sciences Meeting and Exhibit, Reno, NV 2005.

[7] Collis, D. C. and Williams, M. J., "Two-Dimensional Convection from Heated Wires at Low Reynolds Numbers" Journal of Fluid Mechanics, Vol. 6, 1959, pp. 357 – 389.

3 Conventional-statistics Results and Discussion

This chapter contains a discussion of the velocity-field data, focusing on conventional statistics. Conventional statistics convey information concerning the long-time-average characteristics of the flow field, which helps to identify any major changes that occur in the flow under the forcing conditions.

Hereafter, reference will be made to "unforced" and "forced" cases extensively. The "unforced" case refers to the natural flow over the test geometry without any externally applied perturbations; this will act as the base line against which to compare the forced results. The "forced" case refers to the condition when the resonator is being externally driven by the speaker producing an unsteady jet that perturbs the flow, changing its structure. In this and the following chapter, results are provided to examine how the resonator's disturbance affects the flow field.

3.1 Mean Velocity

Figure 3.1 shows normalized mean-velocity contours plotted with the y/h position shown on the vertical axis and x/h position given on the horizontal axis. These plots were generated by averaging the hotwire, time-series data at every location and dividing by the freestream velocity obtained using the pitot tube. Normalizing the data should remove any errors that result from the small deviations in free-stream velocity between sampling locations.

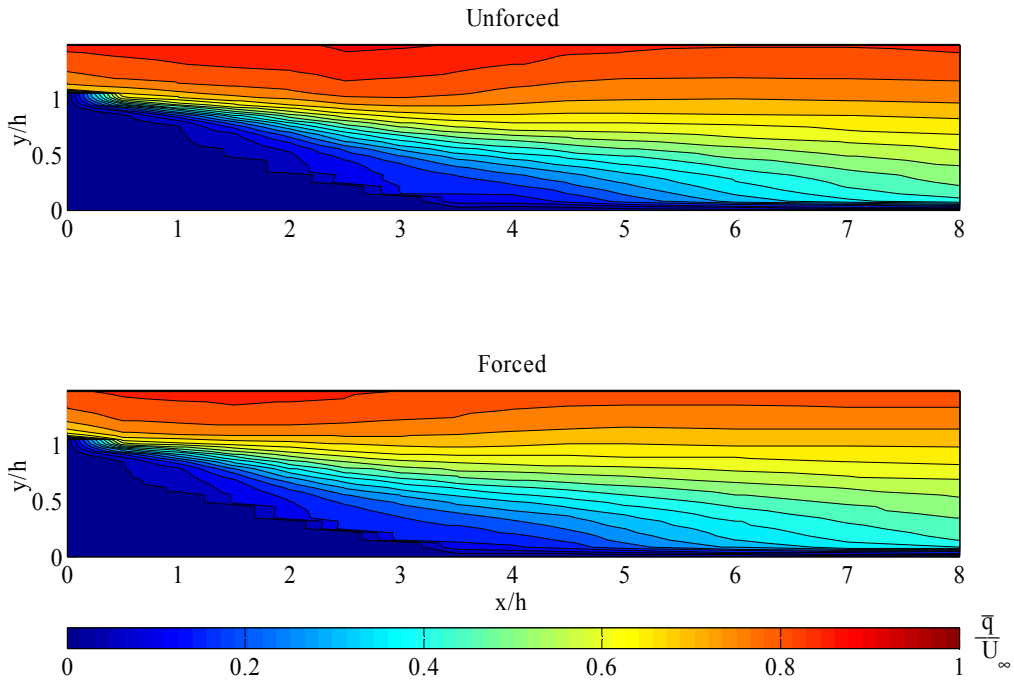

Figure 3.1 Normalized mean-velocity plots

Although the mean-velocity contours for the unforced case look similar to the forced case, there are a few subtle differences. By comparing the velocities at separation, x/h = 0, the y location of the same-color contours (i.e., the same velocity magnitude) for the forced case are located at higher y locations than the unforced case. This may be seen more clearly in Figure 3.2 where line plots are made of the mean-velocity profile at selected x/h locations. It is believed that the upward shift in the velocity profile in the forced case is associated with enhancement in the momentum transport in the y direction, caused by the streaming motion introduced by the control jet. Another interesting point is that in both cases, high-velocity fluid at the top of the measurement domain seems to "dip" into the test region. This may be visualized with the aid of the dark red contour at

the top of the plots in Figure 3.1, in the region of $0.5 \leq x/h \leq 4$. For the forced case this dip happens closer to the point of separation.

Another difference may be found in the region: $1 \leq x/h \leq 5$. In this region, it appears that the shear layer is spreading faster in the forced case. The spreading of the shear layer can be seen more clearly from the profile line plots in Figure 3.2. For example, if one locates the outer edge of the shear layer, say, at $\overline{q}/U_\infty = 0.8$, it is evident from the plots in Figure 3.2 that this would be at a higher y location for the forced in comparison to the unforced case. Alternatively, the width of the shear layer may be linked to the slope of the velocity profile at the inflection point (i.e., maximum velocity gradient); i.e., the vorticity thickness. The steeper this slope, the wider the shear layer. It can be seen that for x/h = 1, both the forced and unforced cases seem to have the same peak velocity gradient, therefore they have the same vorticity thickness near separation. However, at x/h = 3, the forced case has a steeper slope at the inflection point, corresponding to a thicker shear layer. Far downstream of reattachment, x/h = 7, both profiles have the same inflection-point slope, suggesting that the biggest difference between the forced and unforced cases is mostly confined to the flow region upstream of reattachment ($x/h \approx 4$).

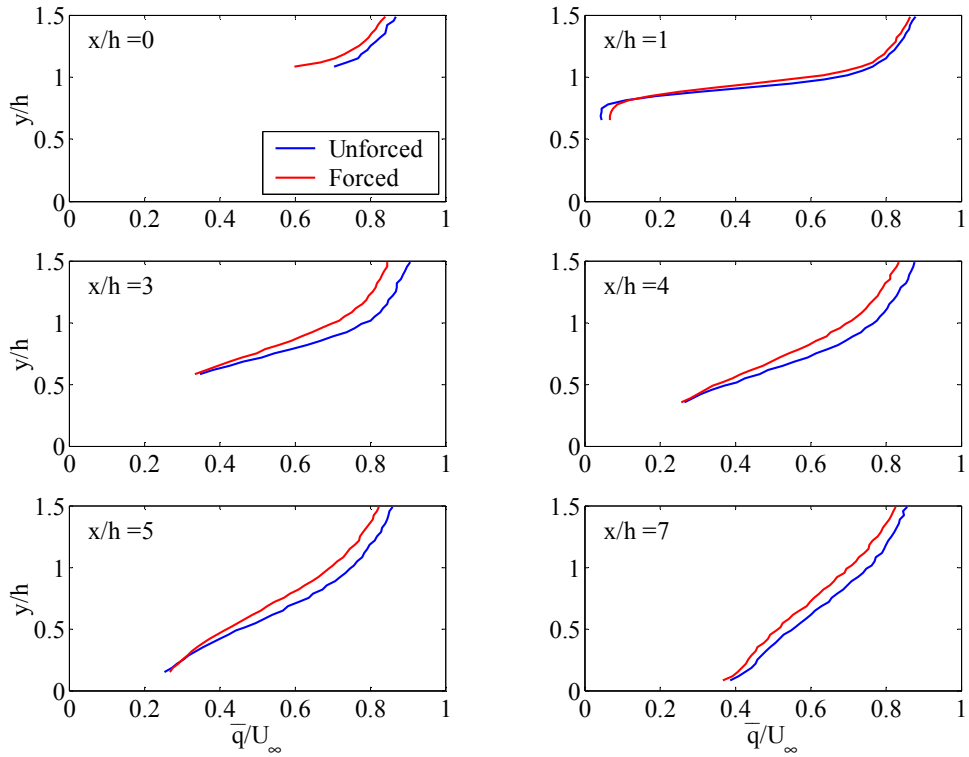

Figure 3.2 Normalized mean-velocity profiles at selected x/h locations

The above suggests that forcing leads to faster development of the shear layer, ultimately leading to shortening of the separation bubble (as reflected in the mean-pressure measurements in Figure 2.13). This is consistent with well-established physics of oscillatory control of separated flows (e.g., Kiya *et. al.*[1], Bhattacharjee *et. al.*[2], and many others).

3.2 Fluctuating Velocity

The strength of the fluctuating (mean-removed) component of velocity (q') is represented by its normalized, root-mean square, or rms, value plotted in Figure 3.3, with the y/h position given on the vertical axis and the x/h position shown on the horizontal axis. The

rms plots reveal information about the energy of the turbulent motion in the flow. The results obtained here, for the unforced case, agree well qualitatively with Hudy[3] who measured the velocity using PIV on the same test model under unforced conditions. In Figure 3.3, high rms values are indicated by red and orange contours, while low values correspond to green and blue shades.

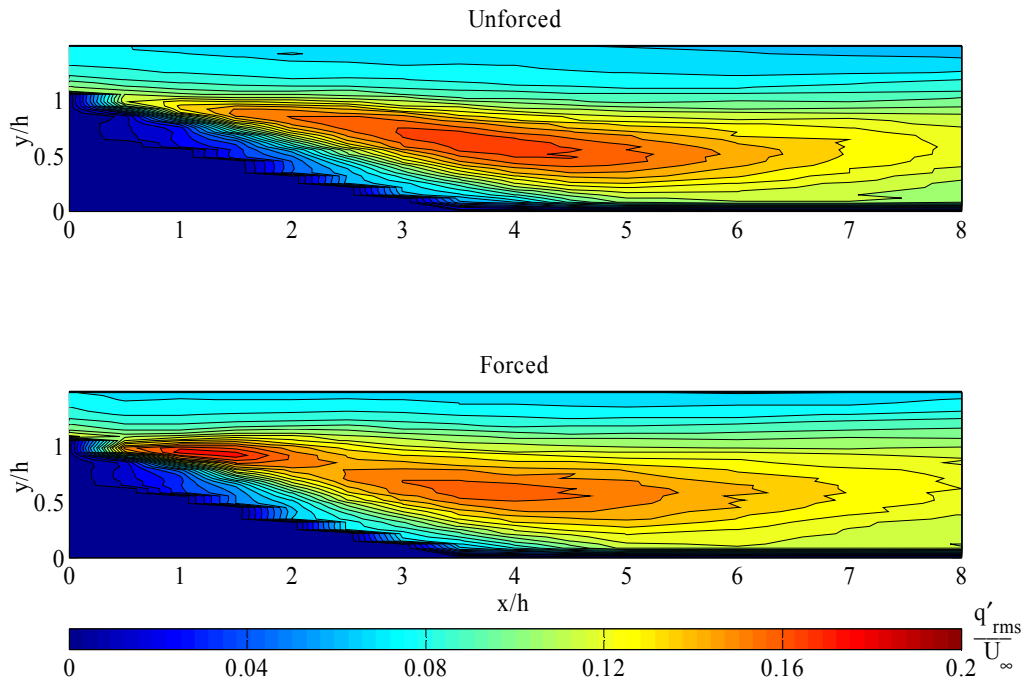

Figure 3.3 Normalized turbulent-velocity rms contour plots

Comparing the unforced and forced rms contour plots, the most noticeable difference is the emergence of a second peak (the first peak being that found near reattachment, $x/h \approx 4$) in the forced case in the region $0.5 \leq x/h \leq 2$ and approximately $y/h = 1$. It will be shown in chapter 4 that the most likely cause of this peak is enhancement of the vertical "flapping" of the shear layer near the point of separation. As previously seen in the mean-

velocity contours, both the unforced and forced rms contour plots seem to be very similar downstream of reattachment. This is interesting because the forcing presumably creates periodic, organized flow structures in the flow. However, the structures apparently dissipate quickly within the separation bubble; thus, they do not affect the flow field downstream of reattachment.

Figure 3.4 shows line profiles of the normalized rms values for the forced and unforced cases at selected x/h locations. The higher rms value near separation (x/h = 1) in the forced case is evident from the figure. Additionally, consistent with the mean-velocity results, the rms data spread over a larger y extent for the forced case, reflecting a larger shear-layer width. Downstream of reattachment, at x/h = 7, the results for both forced and unforced cases are very similar.

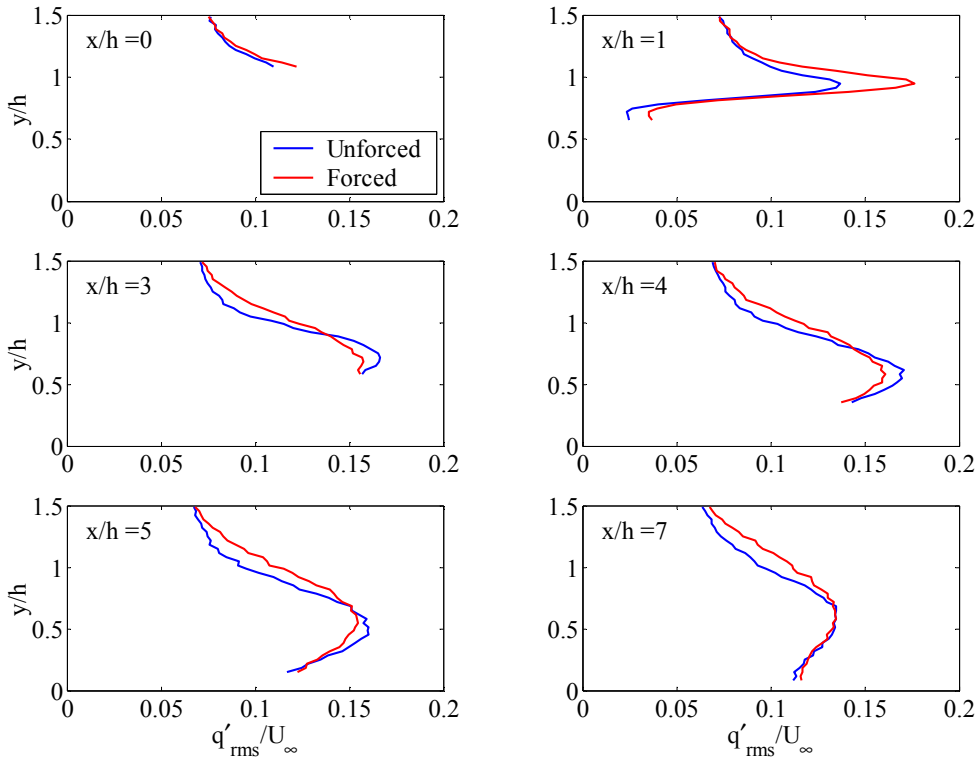

Figure 3.4 Normalized turbulent-velocity rms profiles at selected x/h locations

In many shear-layer studies, such as Castro and Haque[4] as well as Ruderich and Fernholz[5], the lateral (y) location of the maximum rms value at any particular x location is used to mark the center of the shear layer. Using this criterion, the center of the shear layer for both the unforced and forced cases is plotted in Figure 3.5. There appears to be very little difference in the location of the center of the shear layer between the forced and unforced case.

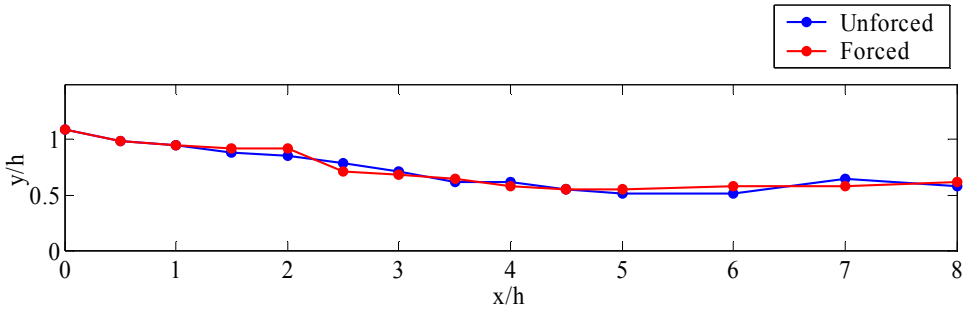

Figure 3.5 Peak q'_{rms} location at different streamwise positions

In addition to inspection of the rms profiles at selected x locations, it is instructive to examine streamwise evolution of the maximum q' rms values. These results are shown in Figure 3.6. For the unforced case, the peak-rms magnitude increases from the point of separation to approximately reattachment (x/h ≈ 4) where it peaks, then decays farther downstream. The forced case does not follow this pattern; instead, the peak-rms value peaks just after separation at x/h = 1, then rapidly decays to a local minimum. Downstream of this minimum, the curve follows the same trend as the unforced case, slowly building to a local peak around reattachment and then decaying. The initial peak in the forced case, found just downstream of separation, is believed to be a product of enhancement in the shear layer flapping and not increase in the energy content of the flow structures. This hypothesis, which originated based on comparison with other studies of oscillatory separation control (to be discussed in Chapter 4), is supported by probability-density-function (PDF) data given later in this chapter and other analyses presented in chapter 4. Another interesting point is that the local maximum that the rms value in the forced case reaches near reattachment is lower than in the unforced case.

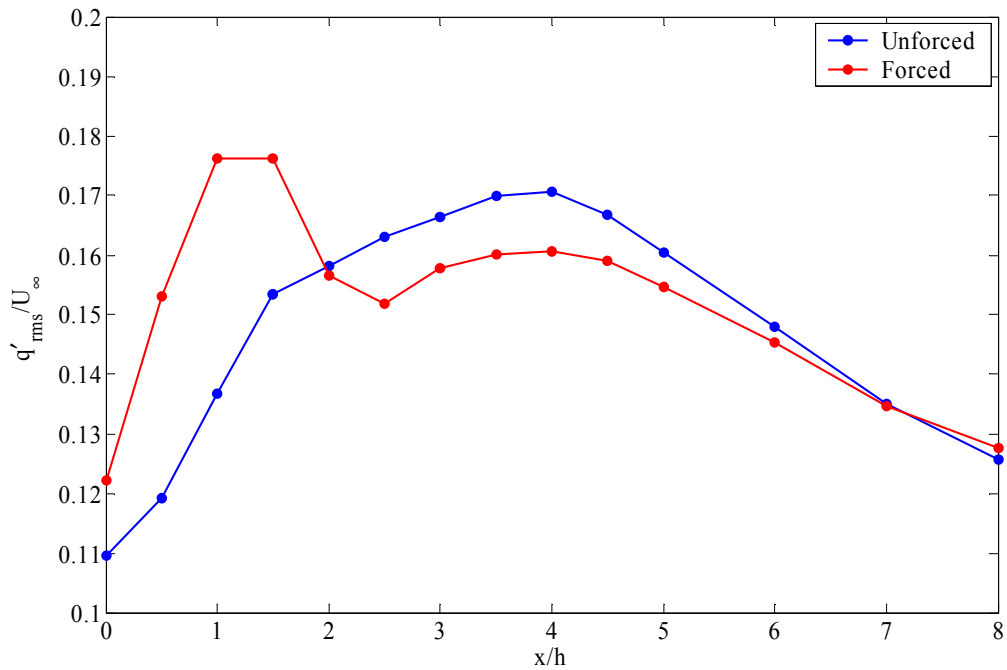

Figure 3.6 Streamwise evolution of the maximum q'_{rms} values

3.2.1.1 Power Spectral Density

The power spectral density (PSD) is a mathematical technique that is used to compute the frequency content of a time series of data. The ability to obtain PSD information is a major advantage of using hotwire over typical Particle Image Velocimetry (PIV) measurements. The hotwire signal captures time-resolved information at a particular, spatial location; whereas PIV yields spatially resolved data at a particular point in time. Figure 3.7 and Figure 3.8 display PSD plots at selected x/h locations for the unforced and forced-flow cases respectively. The PSD values are normalized by the freestream velocity and the step height and plotted on the vertical axis versus the normalized frequency (Fh/U_∞), on the horizontal axis. The different color lines in each plot represent

the 44 different y/h locations where velocity data were taken.

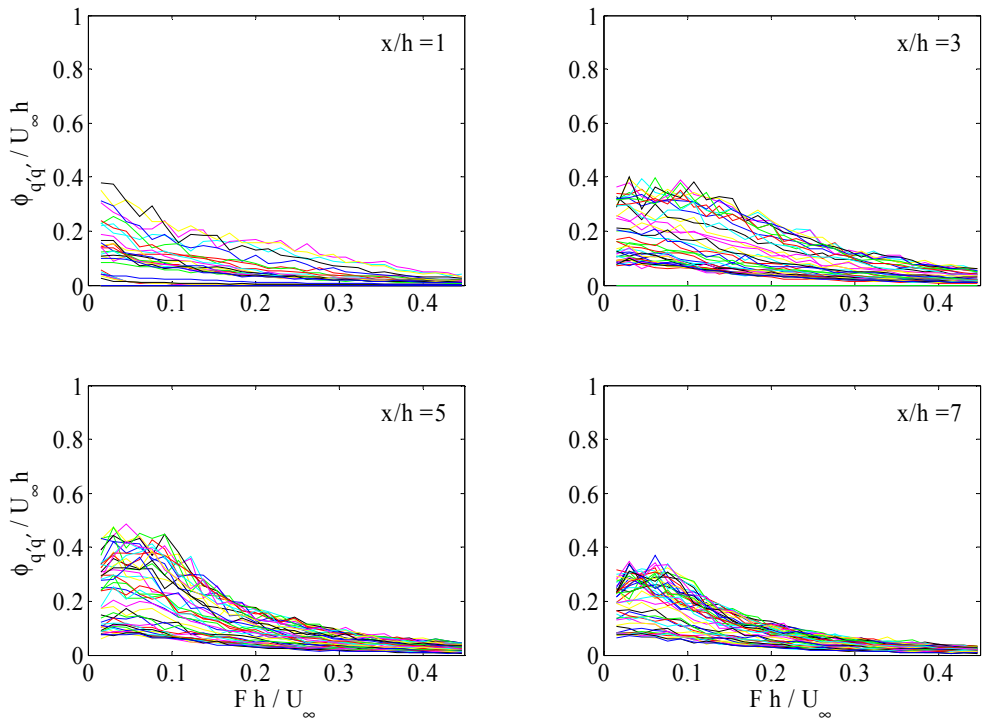

Figure 3.7 Power spectral density of q' for the unforced flow at selected x/h locations

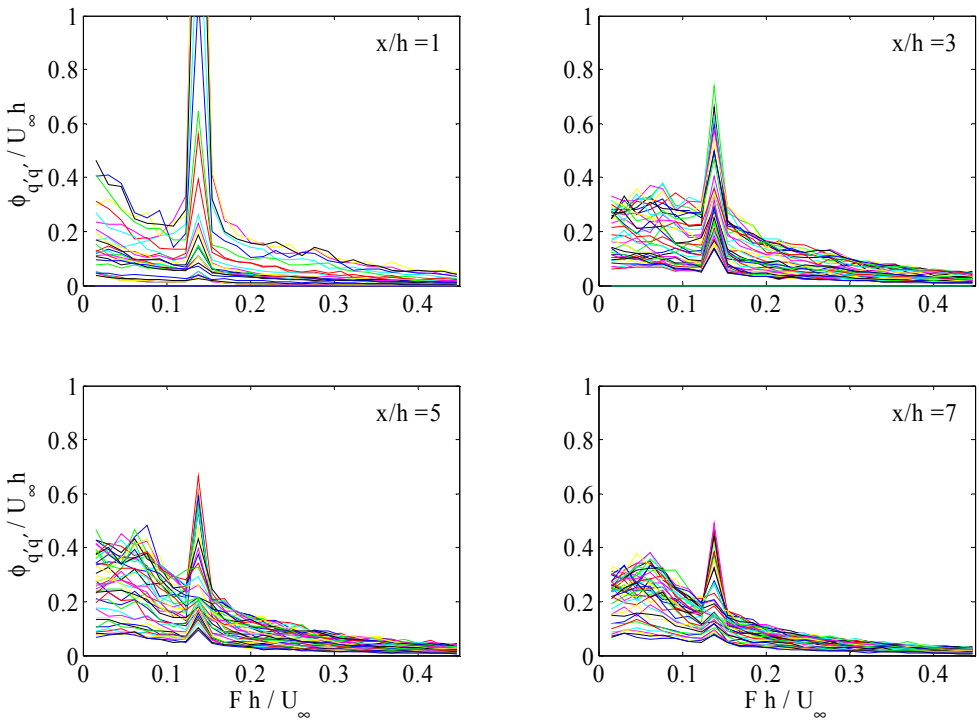

Figure 3.8 Power spectral density of q' for the forced flow at selected x/h locations

The large harmonic peak in Figure 3.8 at x/h = 1 corresponds to the forcing frequency (Fh/U_∞ = 0.1385 or F = 36 Hz). Close to the forcing location (i.e., near separation) q' is dominated by the fluctuations at the forcing frequency. The farther downstream from the forcing location, the less dominant are the velocity fluctuations at the forcing frequency. Upstream of reattachment (x/h ≈ 4), the frequency content of the unforced flow exhibits a broadband character, with no significant peaks. However, downstream of reattachment a broad peak begins to emerge in the frequency range Fh/U_∞ = 0.02 – 0.1, which corresponds to 5 - 25 Hz. By x/h = 7, the peak is very noticeable and is believed to correspond to the 'natural', or preferred, frequency of the flow (i.e., the frequency corresponding to the passage of the shear-layer vortices in the absence of forcing). This

is interesting because a broad peak in the same frequency range is also found for the forced flow. In this case, the peak is better defined and is found to correspond to the 1st sub-harmonic (i.e., half) of the forcing frequency. This harmonic link to the natural frequency of the flow is possibly tied to why 36 Hz was found to be the optimum forcing frequency of the flow. This result agrees with Chun and Sung[6], who used sinusoidal forcing at the point of separation over a backward facing step. They also found the optimal forcing to be twice that of the natural frequency of the flow.

To identify the y location where the velocity fluctuations at the forcing and natural frequencies are dominant, normalized PSD results are plotted verses y/h for selected x/h locations using flooded, color, contour maps in Figure 3.9 and Figure 3.10 for the unforced and forced flow respectively. The PSD contours show that a broad spectrum peak is found in both the forced and unforced cases downstream of reattachment. As discussed earlier, the frequency of the peak is more well defined for the forced flow, and is found centered around a y/h location just above 0.5 for x/h = 5 and 7. Referring to Figure 3.5, it is seen that this location corresponds to the center of the shear layer at the given streamwise positions.

The PSD contour maps for the excited flow show the harmonic peak at the excitation frequency (as seen earlier in the PSD profiles). The y location at which the peak is strongest appears to be near the center of the shear layer at x/h =1. Further downstream this location is closer to the surface of the model: at x/h = 3 the peak has migrated to y/h ≈ 0.5. After reattachment, x/h = 7, the peak is found near the wall, well below the shear-layer center.

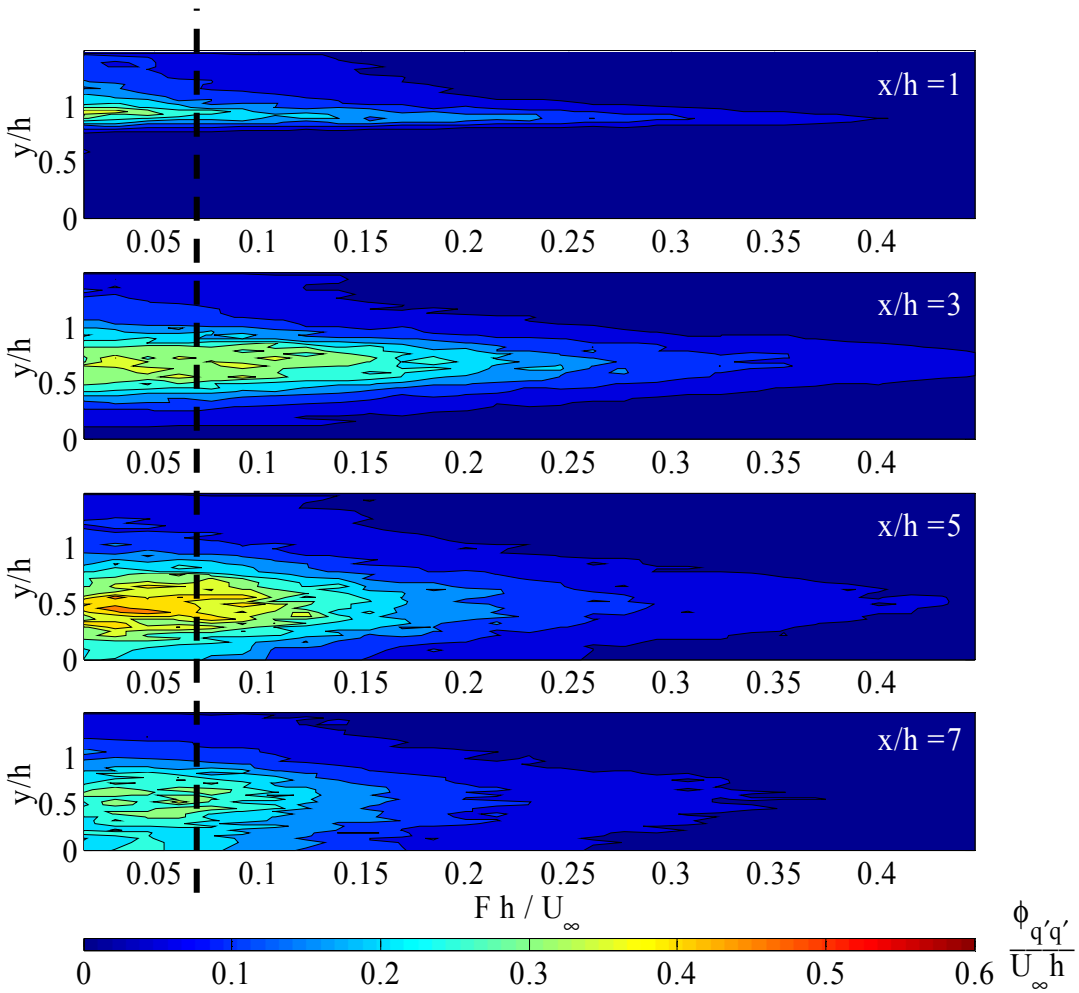

Figure 3.9 Power spectral density of q' for the unforced flow at Selected x/h Locations (broken line shows sub-harmonic of the forcing frequency)

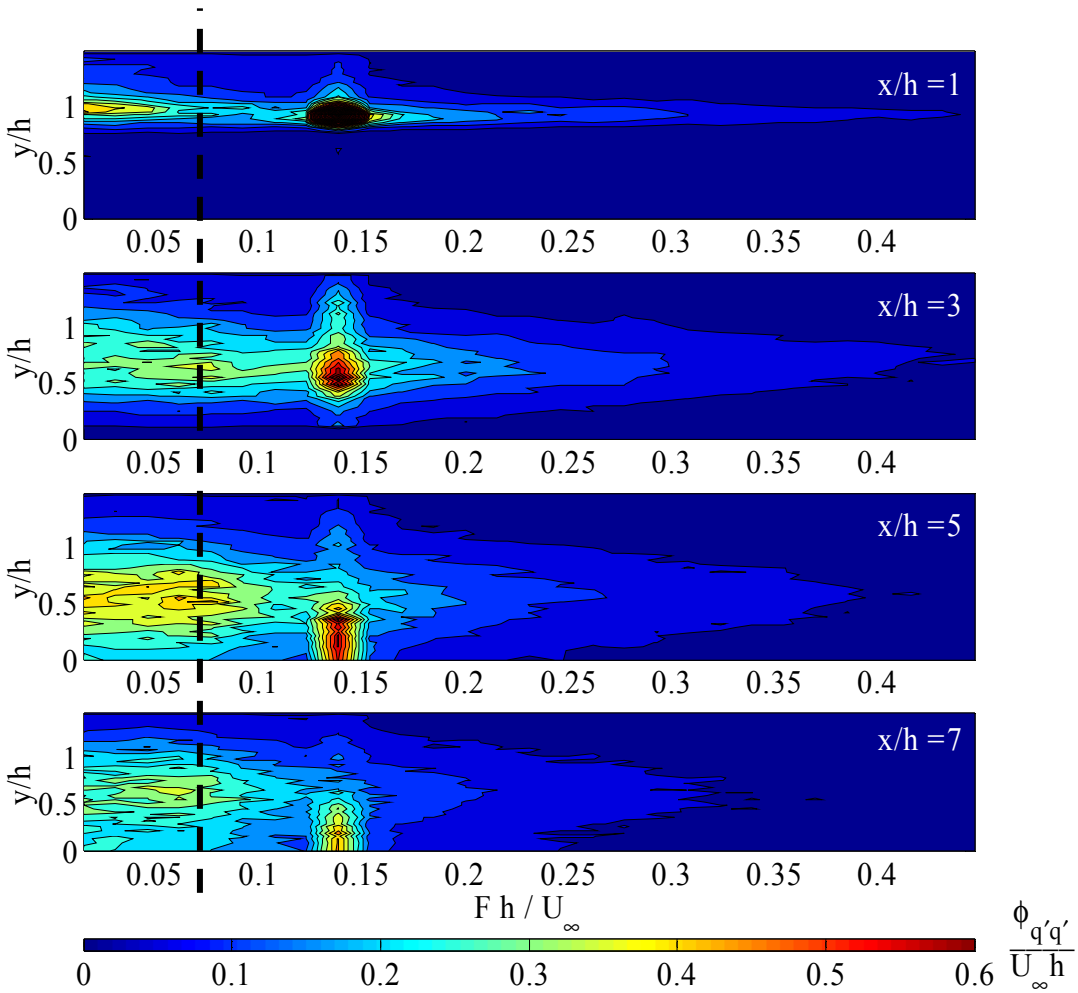

Figure 3.10 Power spectral density for the forced flow at selected x/h locations (broken line shows sub-harmonic of the forcing frequency)

3.3 Velocity Probability Density Function

Velocity probability density function, or PDF, is used to determine the probability that the velocity would assume a value in a particular range at a given location in the flow. Figure 3.11 shows PDF results obtained from data acquired at x/h = 1.5. This streamwise location is chosen because it falls in the region where the near-separation peak is found in the q' rms results of the forced flow (see Figure 3.3 and Figure 3.6). Figure 3.11 contains

(a) a partial time-series trace of the velocity time series for the unforced case, (b) a partial time-series trace of the velocity for the forced case, and (c) the PDF's for both forced and unforced cases. Figure 3.11 shows data for y/h = 0.6833 (which is near the low-speed edge of the shear layer). Both velocity traces are plotted with velocity magnitude on the vertical axis and time on the horizontal axis. The PDF is plotted with probability on the vertical axis and velocity magnitude on the horizontal axis.

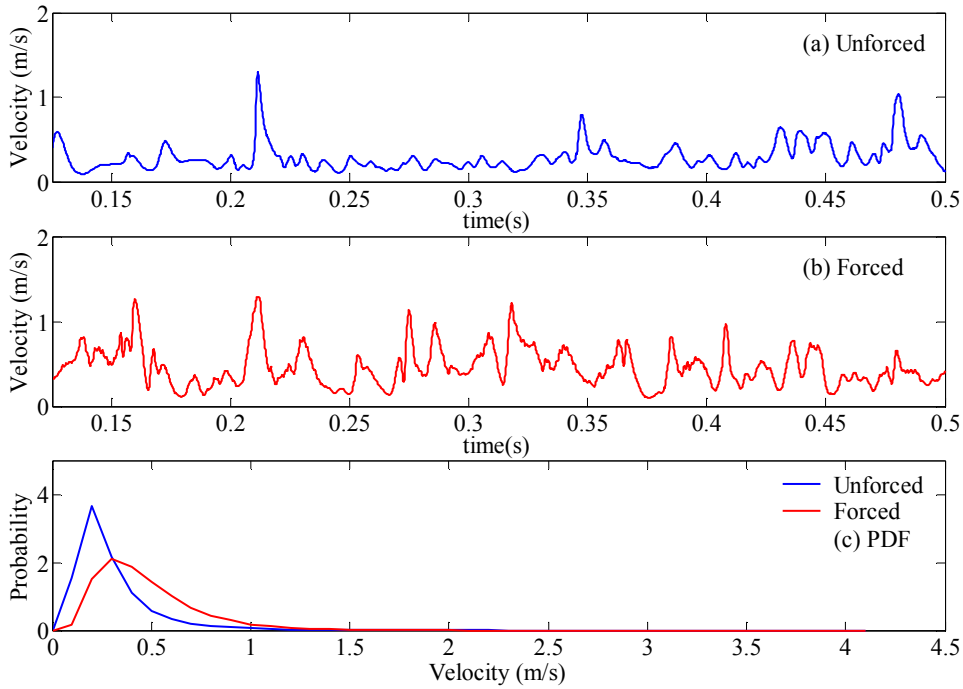

Figure 3.11 Velocity properties at y/h = 0.6833 and x/h = 1.5: (a) sample velocity trace for unforced case, (b) sample velocity trace for forced case, (c) PDF's

Inspection of the hotwire trace for the unforced case in Figure 3.11, shows that the velocity magnitude is low most of the time but spikes to high-magnitude velocity occasionally. It is hypothesized that these spikes are produced when the shear layer "dips" downward (as a result of flapping at separation) and brings higher-velocity fluid in

contact with the hotwire sensor. Under forcing conditions, the hotwire trace is seen to exhibit these spikes more frequently (middle plot in Figure 3.11), suggesting that the flapping of the shear layer is more energetic, bringing the higher-speed fluid in contact with the hotwire more frequently. This results in an increase in the skewness of the PDF in the positive direction, with the PDF for the forced case showing a longer tail at large values of the velocity in comparison to the unforced case. These observations support the idea that the q' rms peak found near separation when forcing the flow is likely associated with enhanced vertical flapping of the shear layer.

3.4 References

[1] Kiya, M., Shimizu, M., Mochizuki, O., "Sinusoidal Forcing of a Turbulent Separation Bubble", Journal of Fluid Mechanics, Vol. 342, 1997, pp. 119-139.

[2] Bhattacharjee, S., Scheelke, B., Troutt, T., "Modification of Vortex Interactions in a Reattaching Separated Flow", American Institute of Aeronautics and Astronautics Journal, Vol. 24, No. 4, July 1986, pp. 623 – 629.

[3] Hudy, L. M., "Simultaneous Wall-Pressure and Velocity Measurements in the Flow Field Downstream of an Axisymmetric Backward Facing Step", PhD. Dissertation, Michigan State University, 2005.

[4] Castro, I. P., and Haque, A., "The Structure of a Turbulent Shear Layer Bounding a Separation Region", Journal of Fluid Mechanics, Vol. 179, 1987, pp. 439-468.

[5] Ruderich, R., and Fernholz, H. H., "An Experimental Investigation of a Turbulent Shear Flow with Separation, Reverse Flow, and Reattachment", Journal of Fluid Mechanics, Vol. 163, 1986, pp. 283-322.

[6] Chung, K., and Sung, J. "Control of Turbulent Separated Flow Over a Backward-Facing Step by Local Forcing", Experiments in Fluids, Vol. 21, 1996, pp. 417-426.

4 Conditional-average Results and Discussion

This chapter contains a discussion of the velocity-field results obtained from conditional statistics. Conditional statistics are employed in this investigation to decompose the hotwire signal according to the triple decomposition introduced by Hussain and Reynolds[1,2]. It is hoped that this will provide further insight into the structure of the flow and shed some light on the mechanism that causes the decrease in size of the separation bubble and reduction in the reattachment length of the forced flow. The conditional analysis was performed on the forced-flow case based on the phase of the forcing cycle. Since a similar phase reference did not exist for the natural-flow case, the analysis was not applied to the unforced flow.

4.1 Conditional averaging

Conditional, or phase, averaging is used here to compute an average of q at any particular phase of the forcing cycle and is defined by

$$\langle q(x,t_o)\rangle = \lim_{M\to\infty}\frac{1}{M}\sum_{n=0}^{M-1} q(x,t_o+n\tau) \tag{4.1}$$

where τ is the period of the forcing signal (half the modulation period in this study), shown in the top plot of Figure 4.1, M is the number of forcing cycles in a time series, and t_o is a time variable corresponding to a particular phase of the forcing cycle; i.e., $0 \le t_o \le \tau$. Thus, the conditional average may be computed at any particular phase φ ($0^o \le \varphi \le 360^o$) of the forcing cycle by changing t_o.

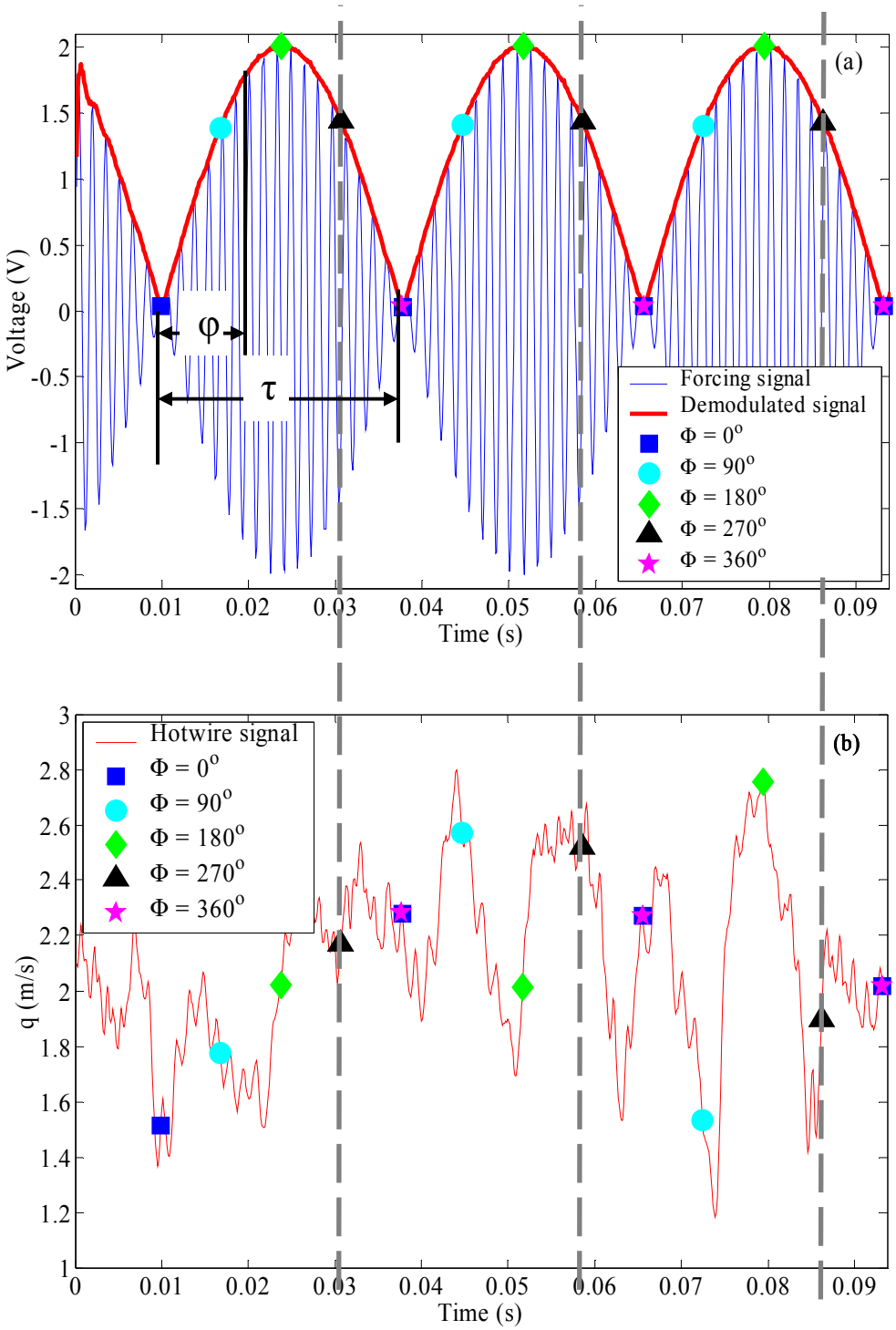

Figure 4.1 Sample time series illustrating different forcing-cycle phases for conditional averaging: (a) forcing signal; (b) flow velocity

Figure 4.1 demonstrates graphically how the conditional average was computed. First, the forcing signal, shown in blue was demodulated, which produced the curve shown by the red line. One cycle of the demodulated signal has a period of τ (which is also the period of the disturbance induced in the flow, corresponding to a frequency of 36 Hz) that can be divided into any number of phases φ. For the current sampling rate of 8000 Hz, one 36 Hz cycle contains approximately 222 data points. Therefore, it was possible to calculate conditional averages for every 1.62° of the flow-excitation cycle.

To select the data point corresponding to a specific phase in different forcing cycles, the start of the cycle (or $\phi = 0^o$) was first identified by marking the minimum point in the demodulated signal (blue squares in Figure 4.1). Knowing that points succeeding the zero-phase point are separated by 1.62^o, it was then possible to pick the point that is closest to the desired phase. It should be evident that the maximum resolution error in locating the desired phase is 1.62^o, or 0.45%.

After determining the data points in the velocity time series corresponding to a particular forcing-cycle phase as seen in Figure 4.1(b), an average of the velocity signal at the selected phase can be computed. For example, black triangle makers are used in Figure 4.1 to identify the forcing cycle phase of 270°. The measured velocity corresponding to this phase occur at time instants that are marked with vertical dashed grey lines in Figure 4.1. By averaging the velocity values for all such time instants, a velocity phase average for 270° is generated for one location in the flow field. This process was repeated for different phases of the forcing cycle and every location where velocity data were

gathered to generate the phase-averaged information.

Normalized, conditional-average velocity contours are plotted with y/h on the vertical axis and x/h on the horizontal axis in Figure 4.2. Note that $\varphi = 0°$ corresponds to the phase where the unsteady jet flow (produced by the resonator) exhibits peak blowing. There are a number of observations that can be made from the conditional-average plots. First, vertical "compressions" and "expansions" of the contours seems to occur successively along the streamwise direction. By examining Figure 4.2 for $\varphi = 0°$, at x/h = 0.5 - 1, the contours are densely packed in the y direction, whereas further downstream at x/h = 1.5 - 2.5 the contours are widely separated in comparison. This pattern seems to repeat farther downstream, forming a wave-like pattern.

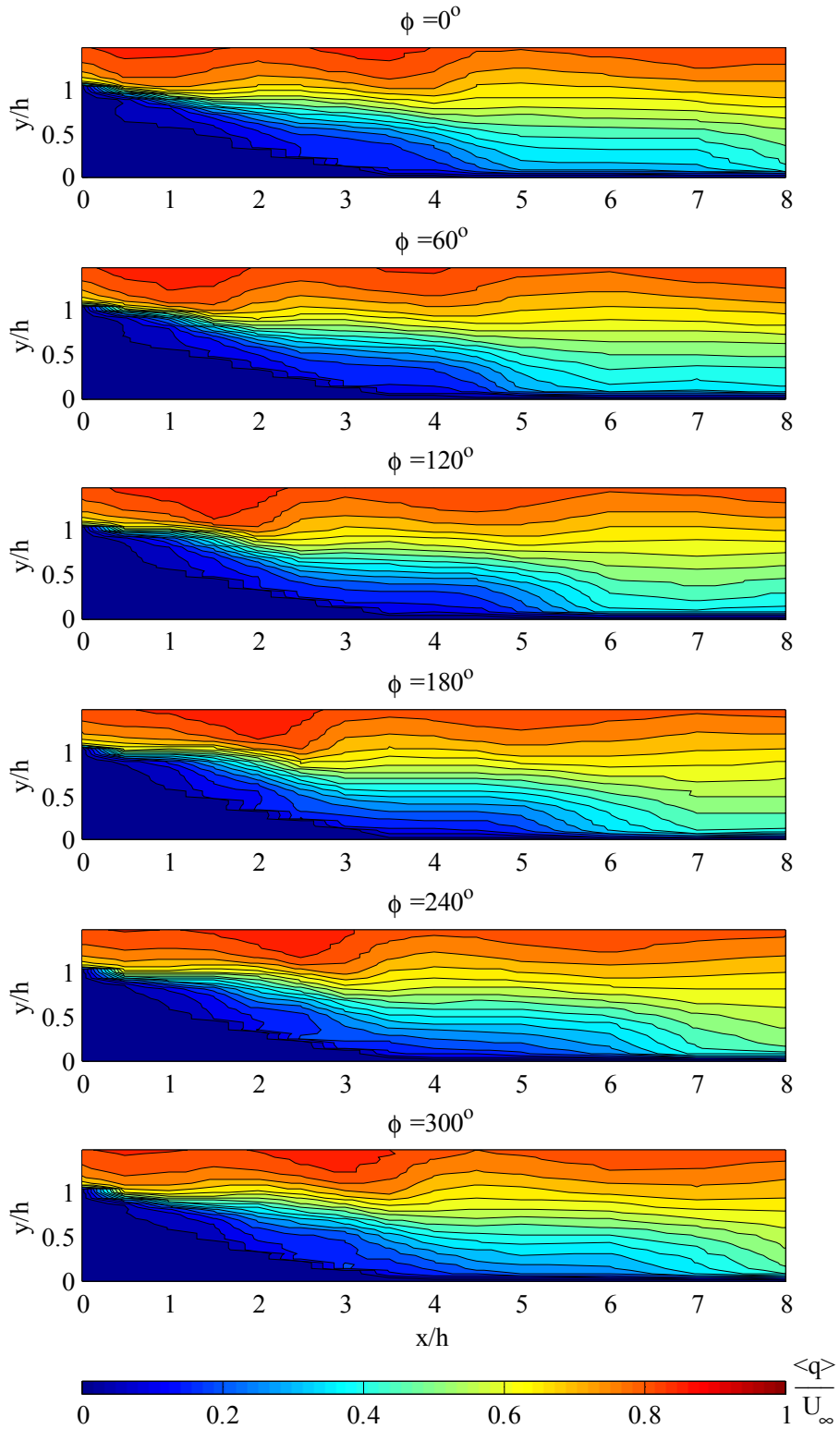

Figure 4.2 Conditional-average-velocity contour plots at selected phases of the forcing cycle

The wavy pattern seems to convect downstream with increasing phase. This may be seen by tracking the center of the first contour compression that starts at x/h = 0.5 for φ = 0. At φ = 120 the compression is found at x/h = 1.5, and finally at φ = 300 it has progressed to x/h = 3. The wave-like disturbance and associated downstream convection implies that the flow control is generating a quasi-periodic coherent structure. These wave-like disturbances have been seen in other experimental and numerical studies by Greenblatt *et.al.*[3] and Rumsey[4] when examining separation control over a wall-mounted hump.

Finally, the <q> results provide additional support to findings in Chapter 3 that suggest the existence of vertical flapping of the shear layer near separation. This becomes clear by following the phase-progression of the contour line that originates from x/h = 0 and y/h ≈ 1.3, marked with a white line in Figure 4.3 that shows a close up of the shear layer in the vicinity of the separation point for the two phases corresponding to the down most and up most excursions of the <q> contours, φ = 0° and φ = 180° respectively. Initially, at φ = 0°, the contour line highlighted with white line in Figure 4.3 has a slope of approximately -0.39. Later in the cycle, at φ = 180°, this contour line is almost horizontal with a slope of approximately -0.1. The implied flapping of the shear layer is believed to be the cause for the q' rms peak seen near separation for the forced flow (see Figure 3.3).

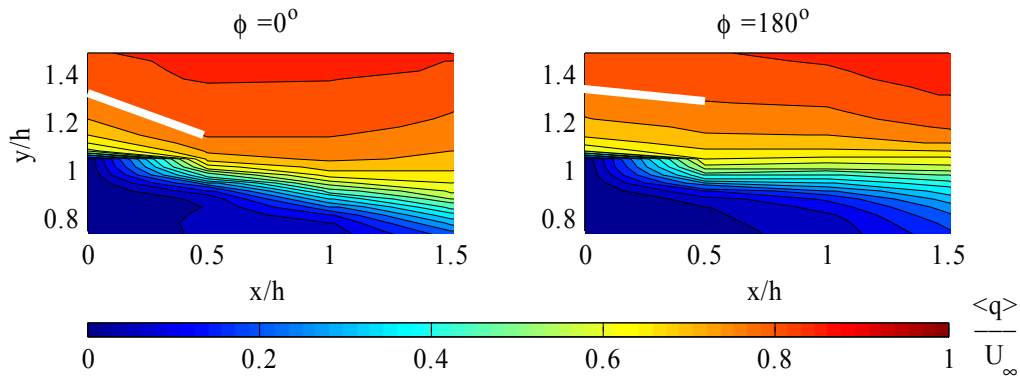

Figure 4.3 Close up of the conditional-average-velocity contour plots in the vicinity of the separation point

A key objective of the present study is to examine whether the nature of the flow structures produced by amplitude-modulated forcing are any different from those found in periodically-excited flows. To this end, it is important to compare the present results with those from an appropriate study involving periodic excitation of a separated flow. The study of Greenblatt *et al.* was selected for this comparison for two reasons: first, the study provided carefully documented, extensive PIV measurements of the flow field; and, second, the data compiled in the investigation are available for public access at http://cfdval2004.larc.nasa.gov/index.html.

The geometry used in the Greenblatt investigation is a wall-mounted, hump model, as seen in Figure 4.4. The oscillatory forcing was generated by an internally driven, zero-mass-flux jet through a slot located at 0.65% chord length (c = 0.42 m) of the model. The velocity field was captured via two-component PIV in three regions (shown in Figure 4.4) downstream of the forcing location, at 36 different phases of the forcing cycle. Here, results from only 4 phases will be used for comparison purposes. Also, the Greenblatt study was conducted at a much higher Reynolds number than the present investigation

(Re_c = 1,114,800 based on chord length and Re_t =142,670 based on maximum thickness of the hump), and the forcing conditions corresponded to F^+= 0.77 and C_μ=0.110%.

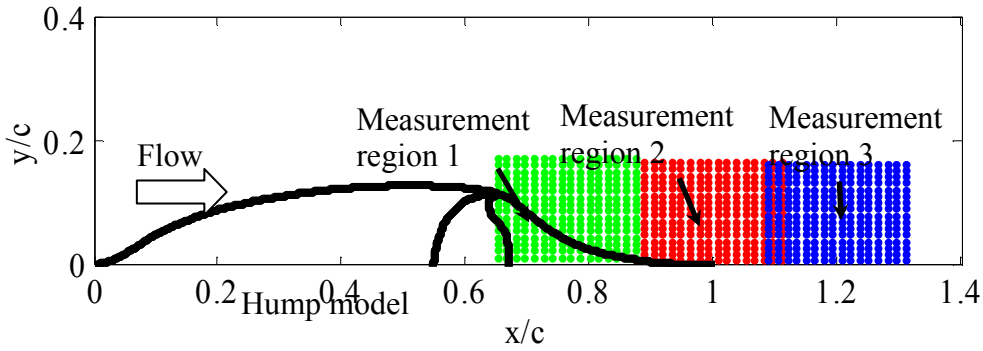

Figure 4.4 Geometry of Greenblatt's hump model and PIV measurement locations

Figure 4.5 provides a comparison between the Greenblatt data and the data obtained in this investigation for the conditional-average of the square of the velocity magnitude ($<q^2>$). Because only certain computed statistics, rather than the raw data, were available from the Greenblatt investigation, <q> could not be obtained. It was possible however to compute $<q^2>$, which is used as the basis for comparison between results obtained from the present and Greenblatt's data (details relating to $<q^2>$ calculation from Greentblatt's data are provided in Appendix A). Note that in Figure 4.5, φ = 0° corresponds to peak blowing of the control jet in both studies. Also, it is helpful to point out that the mean reattachment location for the Greenblatt data is at x/c = 0.94, while in the present study it is roughly estimated to be in the range 3.5 – 4 h based on the mean-pressure measurements.

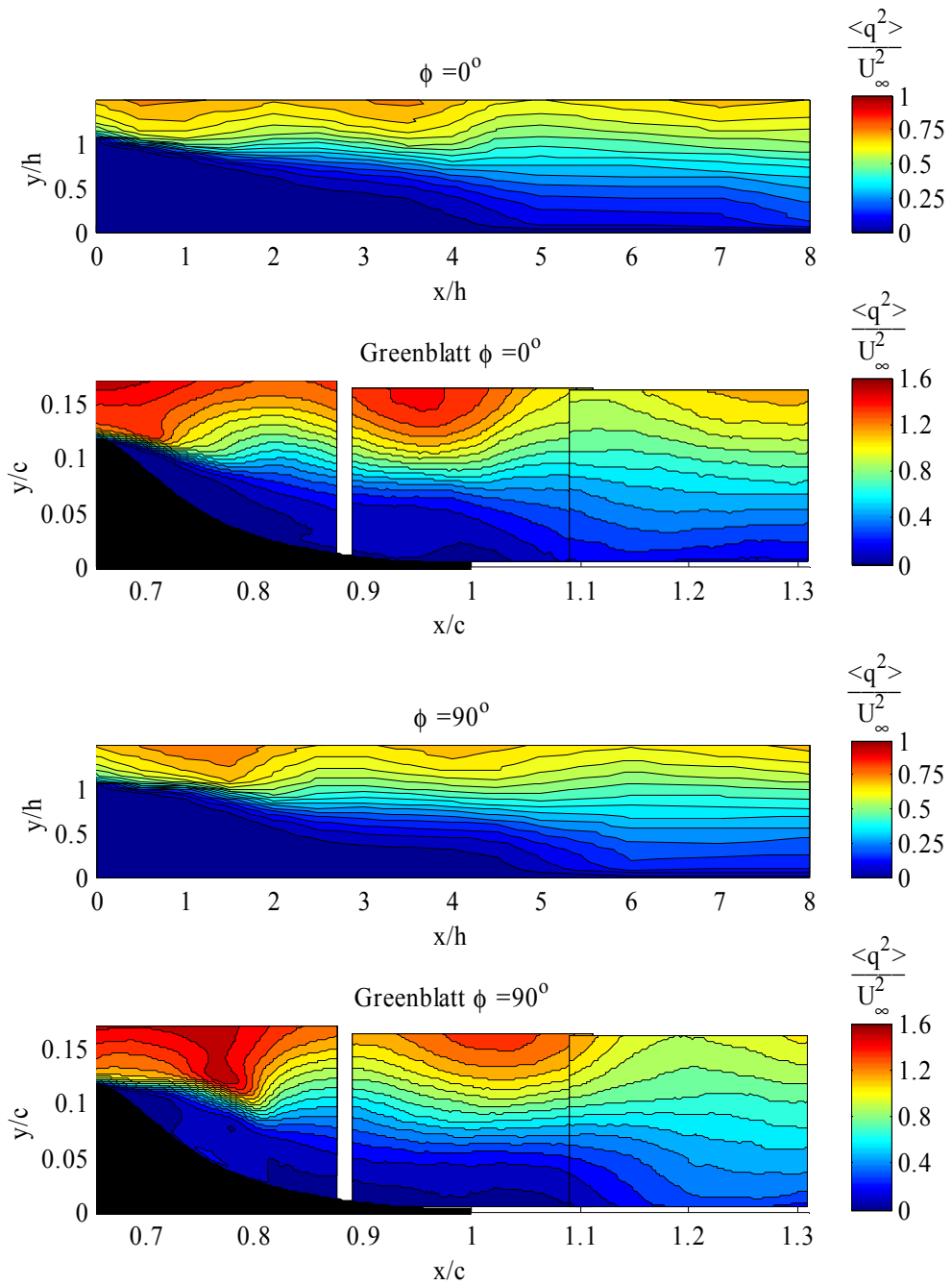
ϕ =0°
y/h
x/h
Greenblatt ϕ =0°
y/c
x/c
ϕ =90°
y/h
x/h
Greenblatt ϕ =90°
y/c
x/c
<q²>/U²∞

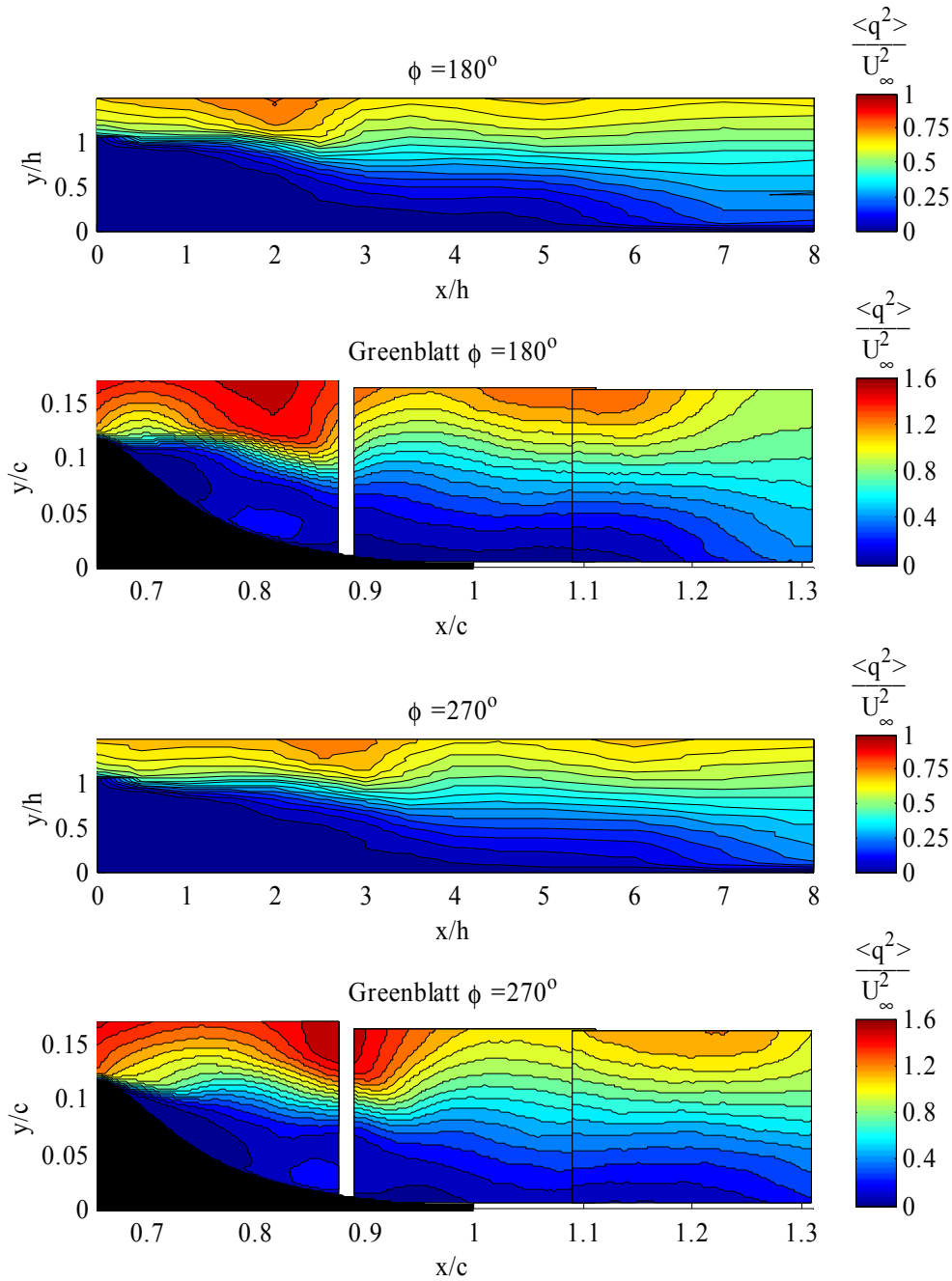

Figure 4.5 Phase-averaged $<q^2>$ contours: comparison of present results with those calculated from Greenblatt's[3] data at selected phases

In Figure 4.5, $<q^2>$ contour maps are plotted above Greenblatt's $<q^2>$ contours for four selected phases of the forcing cycle, φ = 0, 90, 180, and 270. Both contour maps are

plotted as function of the position in the flow, normalized by the step height and chord length for the present and Greenblatt's results respectively.

Inspection of Figure 4.5 shows close, qualitative similarity between the present and Greenblatt's results. In particular, Greenblatt's results also depict the convective, wavy-like disturbance found here. The flapping of the shear layer near the point of separation is also noticeable in the Greenblatt data. This is evident from the movement of the $<q^2>$ contours of the latter case just downstream of separation, as explained earlier in connection with Figure 4.3 (the flapping motion will be observed more clearly below based on vorticity results of the Greenblatt data). Finally, it is also interesting to note that the spatial wavy structures from the Greenblatt data, and the current study, seem to be in phase with each other for similar phases of the forcing cycle. Collectively, the observations derived from Figure 4.5 provide evidence that the flow structures produced by the amplitude-modulated forcing employed here are inherently similar to those produced via the conventional periodic excitation. This is quite useful in the sense that it shows that periodic control of flows could be achieved by low-frequency modulation of actuators that have operating frequency that is substantially higher than the desired control frequency. In other words, the selection and design of an actuator operating frequency may be decoupled and hence becomes unconstrained by the required excitation frequency of the flow.

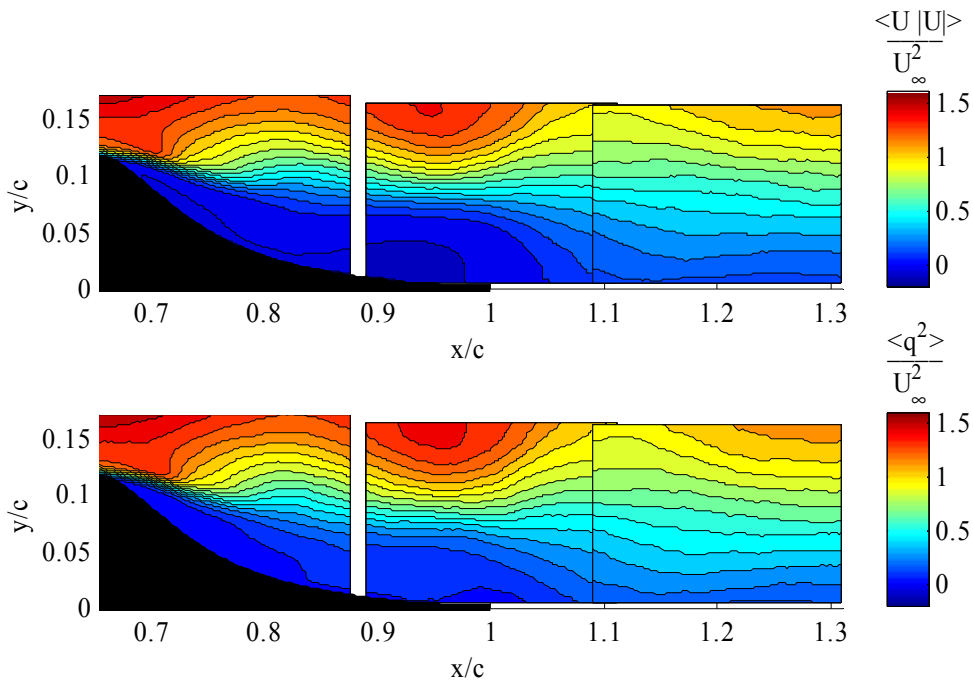

Figure 4.6 Comparison of $\langle U^2\rangle$and $\langle q^2\rangle$ contours at φ = 0° calculated from Greenblatt's data

The Greenblatt data are also helpful in demonstrating that q information is dominated by the streamwise component of the velocity. This is relevant in showing that, for all practical purposes, the present single-wire measurements may be interpreted as a measurement of U, with V having a negligible influence on the outcome. To demonstrate this, Figure 4.6 (top) shows contours of $\langle U*|U|\rangle$ normalized by U_∞^2 while the bottom plot in the figure provides $\langle q^2\rangle$ contours. $\langle U*|U|\rangle$ is plotted instead of $\langle U^2\rangle$ to preserve the direction of the reverse flow region near the surface upstream of reattachment. Both contours were obtained from Greenblatt's data. By comparing the two plots, it is evident that $q \approx U$ is a reasonable assumption for all regions except near reattachment (x/c = 1).

4.2 Triple decomposition

By using a method know as triple decomposition, introduced by Hussain and Reynolds[1,2],

it is possible to decompose the velocity time-series into three, distinct quantities as given by

$$q(x,t) = \overline{q}(x) + \widetilde{q}(x,t) + \hat{q}(x,t) \tag{4.5}$$

where $\tilde{q}$ is the organized-motion, disturbance velocity that is computed form the conditional average using

$$\widetilde{q} = \langle q \rangle - \overline{q} \tag{4.6}$$

and $\hat{q}$ corresponds to the turbulent (random) motion velocity that is obtained from

$$\hat{q} = q(t) - \langle q \rangle \tag{4.7}$$

For the purposes of the present study, one advantage of the triple decomposition is that it provides a means for tracking the evolution of the forcing-induced, coherent structures. To demonstrate this, consider the comparison between the phase-averaged vorticity and $<\hat{u}^2>$ obtained from the Greenblatt data for different phases of the forcing cycle (given in Figure 4.7).

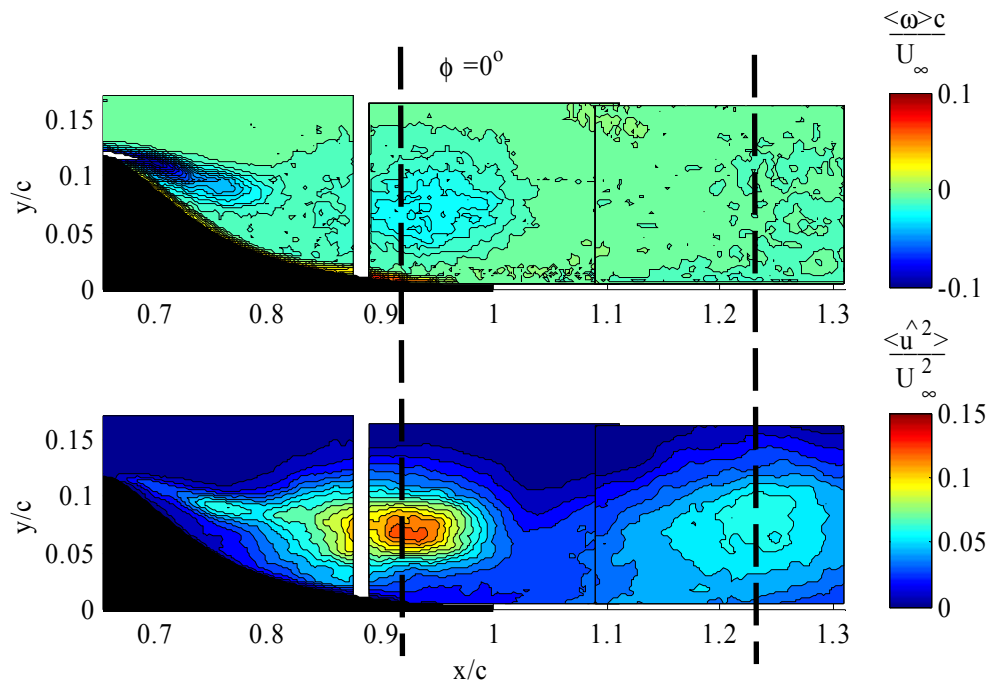
ϕ =0°
<ω>c / U∞
0.1
0
-0.1
y/c
0.15
0.1
0.05
0
0.7
0.8
0.9
1
1.1
1.2
1.3
<u^2> / U∞^2
0.15
0.1
0.05
0
x/c

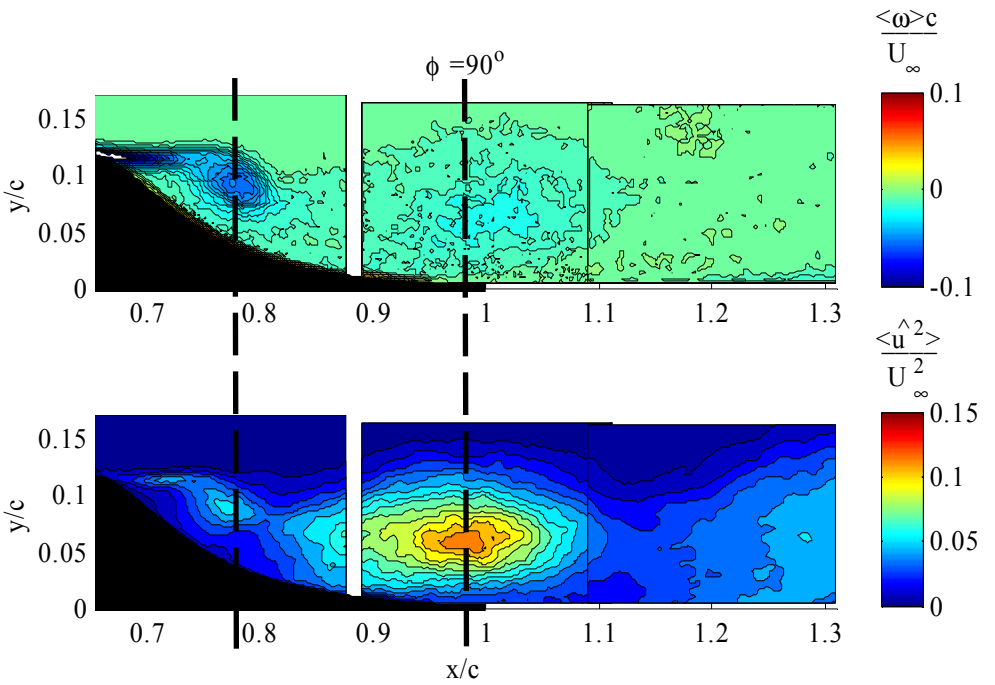
ϕ =90°
<ω>c / U∞
0.1
0
-0.1
y/c
0.15
0.1
0.05
0
0.7
0.8
0.9
1
1.1
1.2
1.3
<u^2> / U∞^2
0.15
0.1
0.05
0
x/c

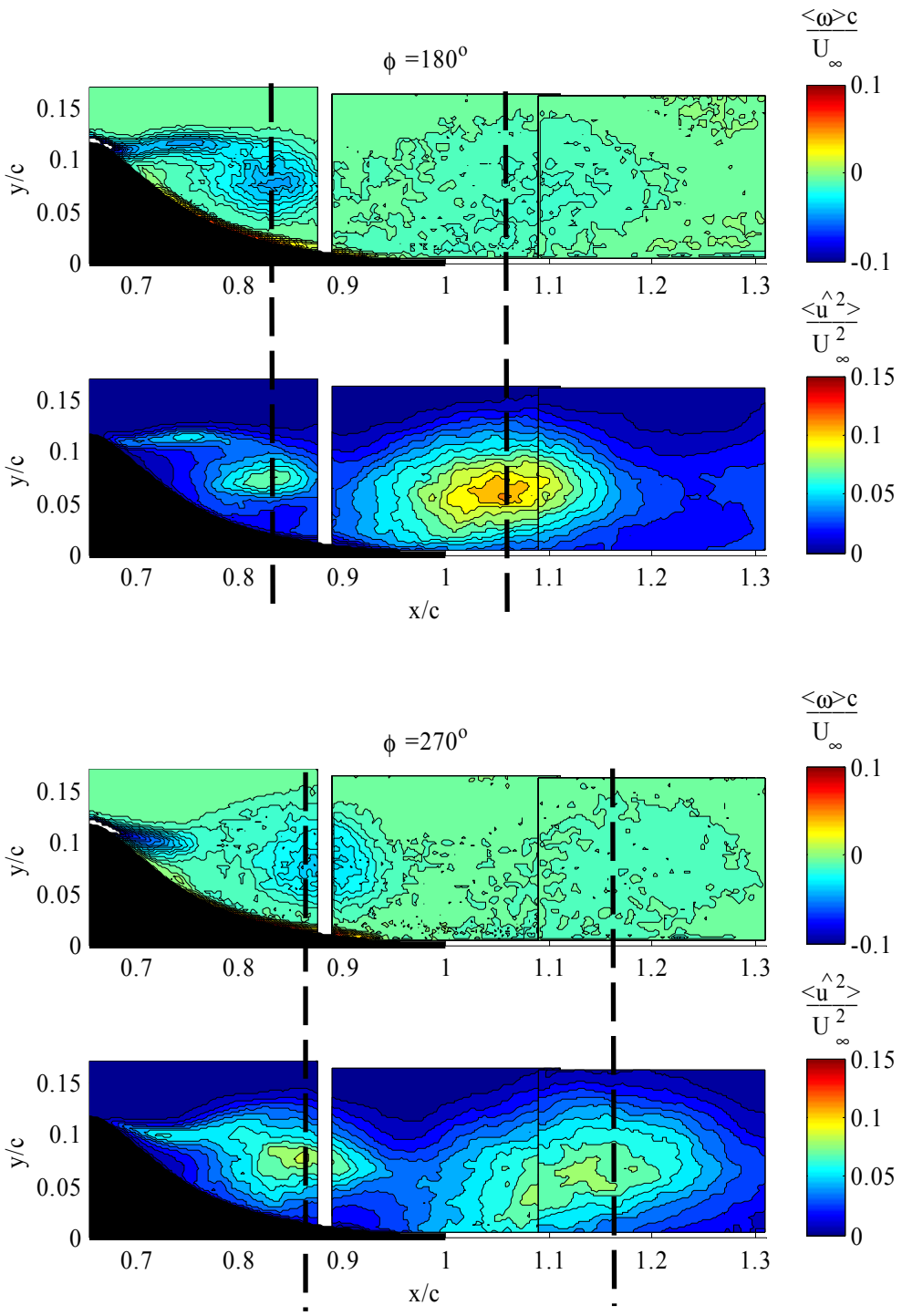

Figure 4.7 Contours of the conditional vorticity, and energy of the streamwise turbulent velocity component, computed from Greenblatt's data for selected phases of the forcing cycle

In Figure 4.7, the normalized vorticity contour maps are plotted above the normalized $<\hat{u}^2>$ contours for four selected phases of the forcing cycle: $\varphi = 0°, 90°, 180°, 270°$; the coordinates for both contour maps are normalized by the chord length. Examination of the vorticity plots reveals the periodic roll-up and subsequent downstream convection of large-scale coherent structures from the initially thin separating shear layer (as identified from the concentration of vorticity. The structures will be referred to as vortex structures with the understanding that, more generally, regions of high vorticity do not necessarily correspond to vortices; Blausius boundary layer is a good example). The streamwise location of the center of the vortex structures is marked with vertical, black, dashed lines based on the vorticity contours. By extending these lines down into the $<\hat{u}^2>$ plot, it is seen that the center of a vortex structure is associated with high $<\hat{u}^2>$ regions. In turn, high $<\hat{u}^2>$ values should result in correspondingly high $<\hat{q}^2>$. Consequently, regions of large $<\hat{q}^2>$ values should be helpful in "tagging" the vortex structures produced by the forcing. This is valuable for the present study, given the lack of vorticity data.

Normalized $<\hat{q}^2>$ velocity contours are plotted in Figure 4.8 for excitation-cycle phases of $\varphi = 0°, 60°, 120°, 180°, 240°$, and $300°$. As explained above, regions of high $<\hat{q}^2>$ will be used to track the evolution of the implied vortex structures that are generated by the forcing. Examination of the results suggests that these structures remain quite small near separation as they convect downstream. Once they reach approximately $x/h = 2$, they appear to grow in the wall-normal direction to approximately the height of the step and continue to travel downstream, this is very similar to what Hudy[5] saw in the unforced case. Beyond reattachment ($x/h \approx 4$) the $<\hat{q}^2>$ signature weakens. This weakening could

be caused by loss of phase locking between the forcing and the induced structures at distances that are far from the point of actuation.

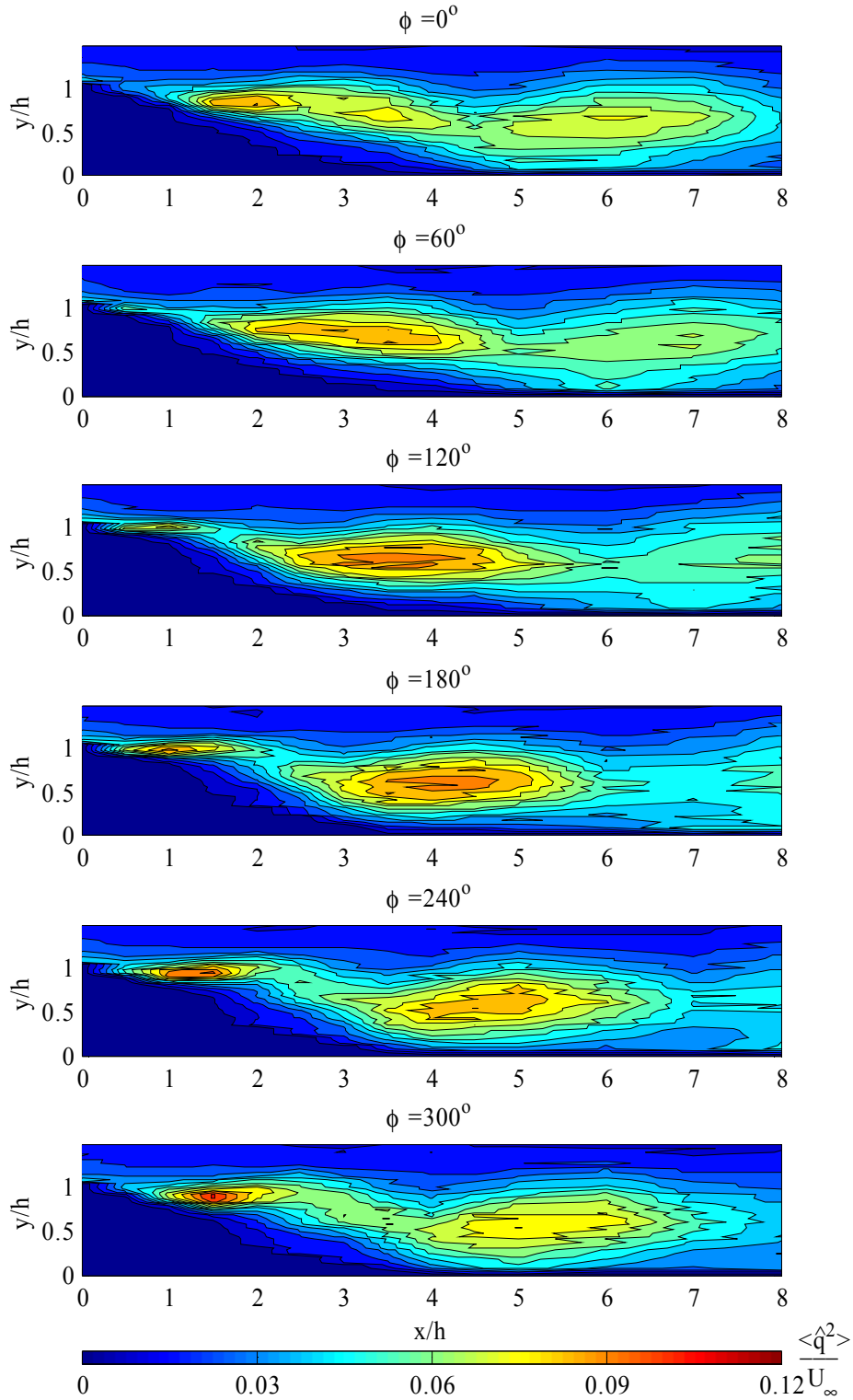

Figure 4.8 $\langle \hat{q}^2 \rangle$ contours for selected phases of the forcing cycle

An estimate of the convection velocity of the flow structures was found by tracking the streamwise location of the peak $<\hat{q}^2>$ value at different phases of the forcing cycle. The results are plotted on an "x-t" diagram using red circles in Figure 4.9. Note that the data have a "staircase" appearance that is caused by the limited streamwise spatial resolution of the measurement grid. A straight line fit to the data was employed to determine the convection velocity. Specifically, the inverse slope of this line is equal to the convection velocity. Note that two different line fits were utilized. First, a line that fits all data points (shown in blue in Figure 4.9) provided an estimate for the convection velocity averaged over the entire measurement domain. However, although this line provides a good description of the data trend for $x/h > 2$, the results for $x/h < 2$ seem to follow a trend with steeper slope than given by the blue line. Therefore, a second line (the green dashed line in Figure 4.9) is used to fit the data in the region $x/h < 2$.

Considering the linear fit to the entire data set, a convection velocity of 1.521 m/s or $0.47U_\infty$ was found. This value agrees closely with the results of Hudy[5] who found the convection velocity at the end of the separation bubble for the unforced flow to be $0.45U_\infty$. Note that Hudy, who conducted her measurements on the same test model as the present one, found this velocity value from tracking the surface-pressure signature. Greenblatt[3] found a slightly slower convection velocity of $0.324U_\infty$. The difference may be related to the difference in test-model geometry.

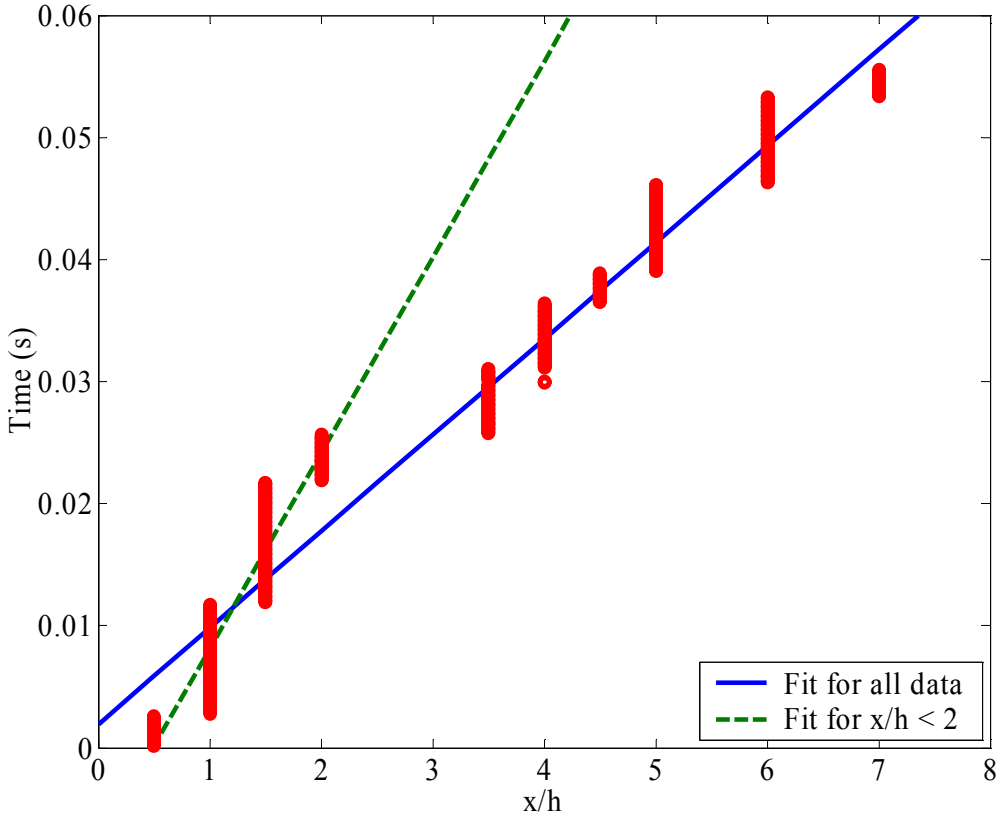

Figure 4.9 Streamwise location of the peak of $<\hat{q}^2>$ at different phases of the forcing cycle. Straight lines represent least-squares fits used to calculate the convection velocity

Near separation (x/h < 2), the convection velocity computed from the green-line fit in Figure 4.7 was 0.75 m/s or $0.233U_\infty$. This suggests that the flow structures have a slower convection velocity up to x/h = 2, then they accelerate to $0.47U_\infty$ farther downstream. It is interesting to note, however, that this change in the velocity takes place in the region 2 < x/h < 4, where Hudy[5] found the shear layer to roll-up into large-scale vortical structures. Thus, it seems that the slower convection velocity is found in a zone upstream of the location of formation of the vortex structures. This is also consistent with the results in Figure 4.8, where there is an abrupt change in the scale of the implied, coherent

structure downstream of x/h = 2.

To further examine the change in the magnitude of the convection velocity, the reader is referred to Figure 4.7 of the conditional-vorticity results computed from Greenblatt's data. Inspection of the vorticity at different phases of the forcing cycle shows the formation of the large-scale vortices to commence at $x/c \approx 0.77$. Upstream of this location, there is no evidence of existence of any vortices. Instead, the region is dominated by the thin, separating shear layer, which exhibits up/down flapping motion throughout the forcing cycle.

The above suggests that the slower convection velocity near separation is more likely an artifact of the velocity signature caused by the flapping of the shear layer. That is, the flapping of the shear layer could create a signature that is commensurate with that of a convecting disturbance. In particular, given two sensors positioned at the same y location in a separating shear layer, one downstream of the other, as the shear layer begins to flap (say moving from its downward most position in the upward direction), the upstream probe will detect the disturbance caused by the shear layer first, followed by the downstream probe at some later time. This time delay would appear to be that of a convecting disturbance.

Another useful result to examine is that concerning the organized component of the triple decomposition (i.e., $\tilde{q}$). This velocity component is displayed for various phases of the forcing cycle in Figure 4.10 with y/h on the vertical axis and x/h shown on the horizontal axis. Note that these results could be obtained from $\langle q \rangle$ data displayed earlier in Figure 4.2 after subtraction of the mean of q. That is, $\tilde{q}$ is essentially the conditional average

of the mean-removed velocity. Generally speaking, it is difficult to deduce the nature of the flow structures in a frame of reference where the local mean is removed (because different parts of the structures appear distorted after removal of the velocity associated with the mean shear). However, $\tilde{q}$ results allow isolation of the organized disturbance that is directly related to the forcing which could shed some light on certain characteristics of the associated flow features.

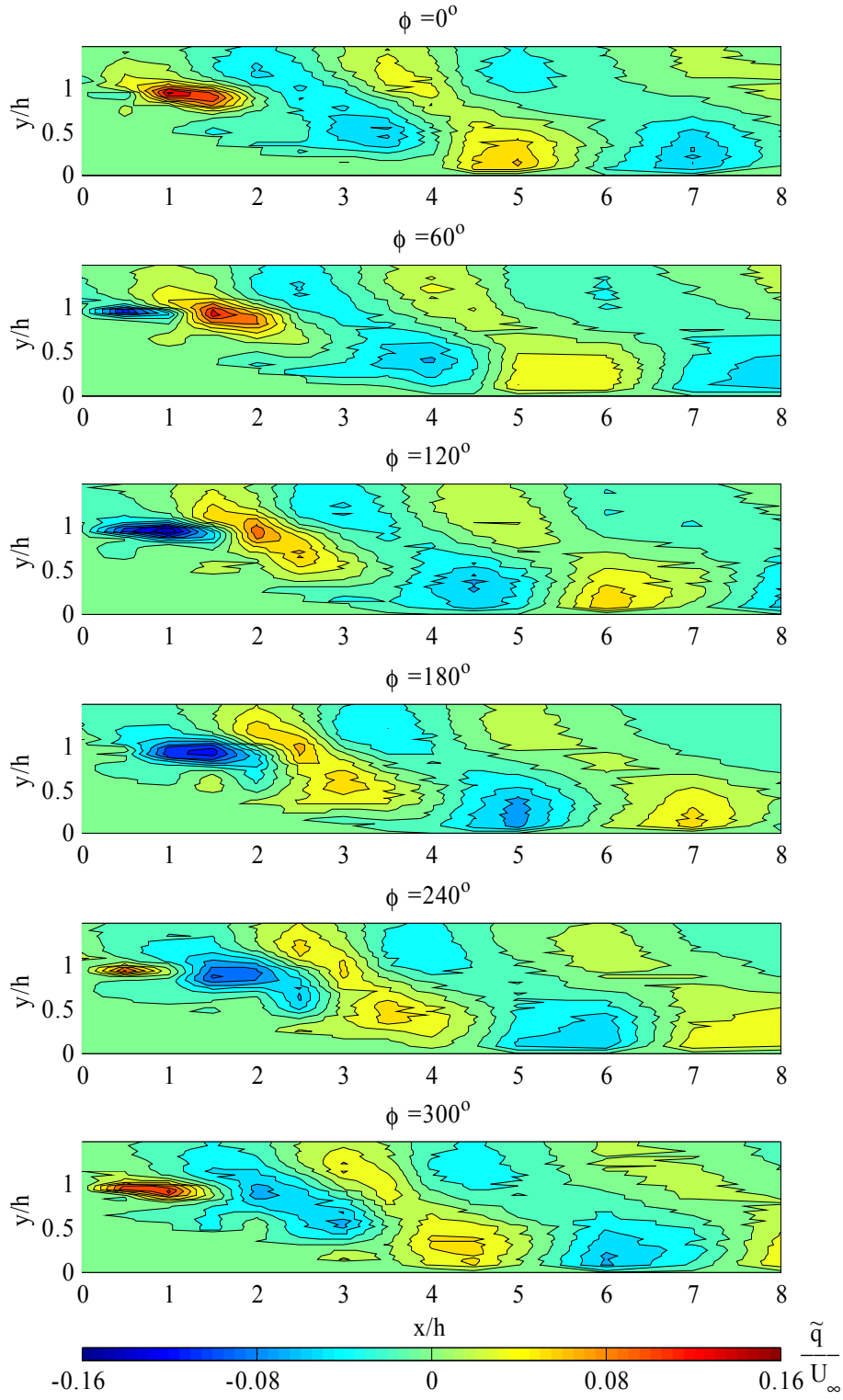

Figure 4.10 q̃ contour plots for selected phases of the forcing cycle

Not surprisingly, examination of Figure 4.8 reveals the evolution of an organized disturbance. The nature of the disturbance is different for $x/h < 2$ in comparison to farther downstream. Within the former domain, the disturbance appears to be concentrated within the thin, separating shear layer. Further downstream, the disturbance spreads substantially in the wall normal direction with the strongest disturbance found in two localized regions: One near the wall, and the other near the top edge of the measurement domain. The sign of the disturbance within these two regions alternates from positive to negative in the streamwise direction, which causes the wave-like appearance discussed earlier in connection with Figure 4.2. It is also notable that the magnitude of $\tilde{q}$ is stronger near the wall than it is close to the top of the measurement domain.

Comparison of the evolution of the random and organized disturbance (in Figure 4.8 and Figure 4.10, respectively) reveals that, for $x/h > 2$, the former is strongest along the center of the shear layer, while the latter makes the most energetic contribution near the edges. This may be seen more clearly by calculating the rms of $\tilde{q}$ and $\hat{q}$, the results of which are displayed in Figure 4.11.

The stronger values of $\tilde{q}$ near the edges of the shear layer is consistent with the idea that the forcing introduces organized, vortex structures, as discussed earlier in connection with the vorticity results based on Greenblatt's data. More specifically, a streamwise-traveling vortex is likely to contribute to the fluctuations of the streamwise velocity (and hence q) strongest towards the edges of the vortex, rather than at the core.

Another interesting observation from Figure 4.11 relates to the rms of the

organized disturbance near the separation point. It is evident that the contours extend over a considerably wider distance in the y direction in comparison to the rms of the random velocity. This is likely a reflection of the enhanced lateral motion of the shear layer (i.e., flapping) in synchronization with the forcing, as discussed previously.

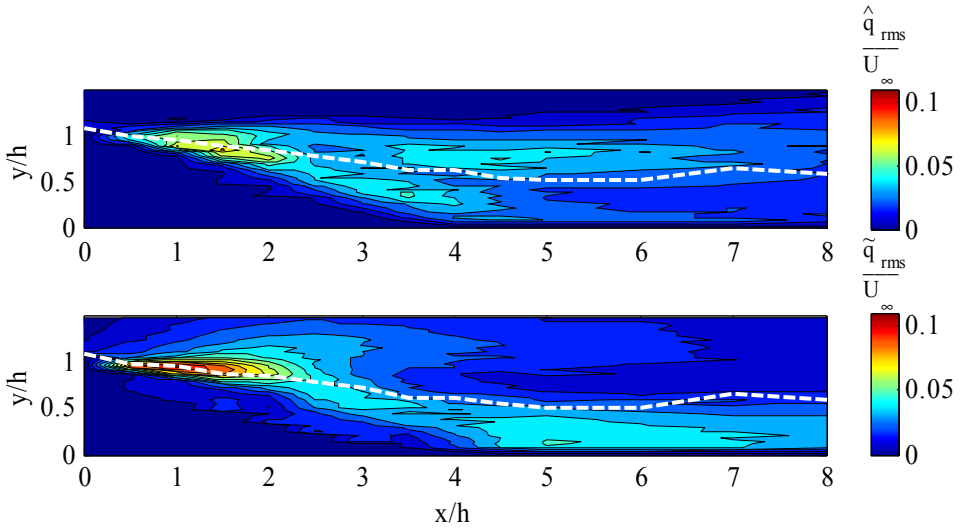

Figure 4.11 rms of the turbulent (top) and the organized (bottom) velocity components. Broken white line identifies the center of the shear layer based on peak q'_{rms}

4.3 References

[1] Hussain, A.K.M.F., and Reynolds, W.C. "The Mechanics of an Organized Wave in Turbulent Shear Flow", Journal of Fluid Mechanics, Vol. 41, part 2, 1970, pp. 241-258.

[2] Reynolds, W.C., Hussain, A.K.M.F. "The Mechanics of an Organized Wave in Turbulent Shear Flow Part 3. Theoretical Models and Comparisons with Experiments", Journal of Fluid Mechanics, Vol. 54, part 2, 1972, pp. 263-288.

[3] Greenblatt, D., Paschal, K., Yao, C., Harris, J., "A Separation Control CFD Validation Test Case Part 2. Zero Efflux Oscillatory Blowing", AIAA-2005-0485 43rd American Institute of Aeronautics and Astronautics Aerospace Sciences Meeting and Exhibit, Reno, NV 2005.

[4] Rumsey, C., "Reynolds-Averaged Navier-Stokes Analysis of Zero Efflux Control over a Hump Model" AIAA-2006-1114 44th American Institute of Aeronautics and Astronautics Aerospace Sciences Meeting and Exhibit, Reno, NV 2006.

[5] Hudy, L. M., "Simultaneous Wall-Pressure and Velocity Measurements in the Flow Field Downstream of an Axisymmetric Backward Facing Step", PhD. Dissertation, Michigan State University, 2005.

5 Conclusions and Recommendations for Future Work

This chapter contains a summary of the work presented in previous chapters and an outline of the major flow-field characteristics downstream of an axisymmetric backward facing step under natural and forced conditions. Also provided here are suggestions for future work that could further the understanding of the topic investigated here.

5.1 Conclusions

The main goal for this investigation was to characterize the flow field downstream of an axisymmetric, backward-facing-step under unforced- and forced-flow conditions. The forcing method was based on the use of a Helmholtz resonator that is externally driven with an acoustic, *amplitude-modulated* disturbance (which was developed by Aditjandra[1]). This forcing system is unique in comparison to the typical direct *harmonic* forcing seen in the literature, to the best of the authors knowledge. Therefore, the present study's primary concern was to address the question of whether amplitude-modulated excitation affected the flow in a manner that is similar to, or different from, conventional oscillatory control. To this end, a single-hotwire sensor was employed to gather velocity information downstream of the axi-symmetric back step. The compiled data were analyzed using conventional and conditional statistics. The results were found to be consistent with those found in the literature for harmonic forcing.

The similarity between amplitude-modulated and conventional harmonic forcing was determined based on detailed comparison of conditional statistics obtained from the present study to those obtained from a database compiled by Greenbalt *et. al.*[2] in a

periodically-excited separation over a wall-mounted hump. Data from both studies verify that large-scale coherent structures are produced regularly during the forcing cycle. These structures are initially produced from the thin shear layer at a location approximately half way to reattachment ($x/h = 2 - 3$) where they grow in size to approximately one-step height and convect downstream.

The contrast in the characteristics of the organized motion produced by the control upstream of $x/h \approx 2 - 3$ and farther downstream is not limited to the scale of the forced disturbance. Additional differences include the convection velocity, which was found to be $0.233U_\infty$ in the former region and $0.47U_\infty$ in the latter. Moreover, the forcing was found to produce a localized peak in the rms of the mean-removed velocity at $x/h = 1.0$. Given that this location is upstream of the location of formation of the large-scale structures, in addition to evidence based on a number of statistical analyses, this peak was attributed to enhancement of the vertical flapping of the shear layer at separation.

Finally, a power spectral density analysis showed that the flow response to the forcing is very strong near the point of separation but it quickly dissipates farther downstream. The analysis also provides insight to the possible reasoning for the selected forcing frequency being the optimal control frequency (as found by Adjeranda[1]). More specifically, the forcing frequency was found to be twice the natural frequency of the flow at the end of the separation zone under unforced conditions. This finding is similar to that found by Chun and Sung[3] who also found the optimal forcing frequency to be twice the natural frequency of the flow.

5.2 Future Work

A few suggestions for extension/enhancement of the present study follow:

- Conduct wall-pressure measurements at the same conditions of the forcing employed here in order to investigate the surface-pressure imprint of the flow structures produced by the forcing. Results from the present investigation could be synchronized with the surface-pressure data through the phase reference of the forcing cycle.

- The above would also allow examination of the utility of stochastic estimation in estimating the flow structures from the unsteady wall-pressure signature under forced conditions. Such an examination could be useful for implementation of feedback control of the separation bubble.

- Conduct the experiment using particle image velocimetry, or laser Doppler velocimetry to capture the details of the velocity field accurately everywhere, including within the re-circulation region and in the vicinity of reattachment.

5.3 References

[1]Aditjandra, A., "Amplitude-modulated Excitation of a Separated Flow Using an Externally Driven Helmholtz Resonator" Masters Thesis, Michigan State University, 2006.

[2] Greenblatt, D., Paschal, K., Yao, C., Harris, J., "A Separation Control CFD Validation Test Case Part 2. Zero Efflux Oscillatory Blowing", AIAA-2005-0485 43rd American Institute of Aeronautics and Astronautics Aerospace Sciences Meeting and Exhibit, Reno, NV, 2005.

[3] Chung, K. and Sung, J. "Control of turbulent separated flow over a backward-facing step by local forcing" Experiments in Fluids, Vol. 21, 1996, pp 417-426

A. Appendix

In the following, a derivation is provided to show how <q^2> was computed from Greenblatt's[1] data

$$\left\langle q^2 \right\rangle = \left\langle u^2 + v^2 \right\rangle \tag{A.1}$$

since summation and averaging are commutative:

$$\left\langle q^2 \right\rangle = \left\langle u^2 \right\rangle + \left\langle v^2 \right\rangle \tag{A.2}$$

decomposing velocities into mean and fluctuating components

$$\left\langle q^2 \right\rangle = \left\langle \left(\bar{u} + u'\right)^2 \right\rangle + \left\langle \left(\bar{v} + v'\right)^2 \right\rangle \tag{A.3}$$

$$\left\langle q^2 \right\rangle = \left\langle \bar{u}^2 + 2\bar{u}u' + u'^2 \right\rangle + \left\langle \bar{v}^2 + 2\bar{v}v' + v'^2 \right\rangle \tag{A.4}$$

because the mean of $\bar{u}$ and $\bar{v}$ are constant quantities

$$\begin{aligned} \left\langle \bar{u} \right\rangle &= \bar{u} \\ \left\langle \bar{v} \right\rangle &= \bar{v} \end{aligned} \tag{A.5}$$

substituting (A.5) into (A.4)

$$\left\langle q^2 \right\rangle = \bar{u}^2 + 2\bar{u}\left\langle u' \right\rangle + \left\langle u'^2 \right\rangle + \bar{v}^2 + 2\bar{v}\left\langle v' \right\rangle + \left\langle v'^2 \right\rangle \tag{A.6}$$

the fluctuating component can be further divided into periodic component and turbulent component

$$\langle u' \rangle = \langle \tilde{u} + \hat{u} \rangle$$
$$\langle v' \rangle = \langle \tilde{v} + \hat{v} \rangle \tag{A.7}$$

or

$$\langle u' \rangle = \langle \tilde{u} \rangle + \langle \hat{u} \rangle$$
$$\langle v' \rangle = \langle \tilde{v} \rangle + \langle \hat{v} \rangle \tag{A.8}$$

noting that

$$\langle \tilde{u} \rangle = \tilde{u}$$
$$\langle \tilde{v} \rangle = \tilde{v} \tag{A.9}$$

and by definition

$$\langle \hat{u} \rangle = 0$$
$$\langle \hat{v} \rangle = 0 \tag{A.10}$$

then (A.8) reduces to

$$\langle u' \rangle = \tilde{u}$$
$$\langle v' \rangle = \tilde{v} \tag{A.11}$$

substituting in equation (A.11) into (A.6) results in $<q^2>$

$$\boxed{\langle q^2 \rangle = \bar{u}^2 + 2\bar{u}\tilde{u} + \langle u'^2 \rangle + \bar{v}^2 + 2\bar{v}\tilde{v} + \langle v'^2 \rangle} \tag{A.12}$$

Beginning with values that are available from Greenblatt's database, <u> and <v>,

and expanding into mean and fluctuating components

$$\langle u\rangle^2 + \langle v\rangle^2 = \langle \bar{u} + u'\rangle^2 + \langle \bar{v} + v'\rangle^2 \tag{A.13}$$

$$\langle u\rangle^2 + \langle v\rangle^2 = \bar{u}^2 + 2\bar{u}\langle u'\rangle + \langle u'\rangle^2 + \bar{v}^2 + 2\bar{v}\langle v'\rangle + \langle v'\rangle^2 \tag{A.14}$$

substituting equation (A.11) into (A.14) results in

$$\langle u\rangle^2 + \langle v\rangle^2 = \bar{u}^2 + 2\bar{u}\tilde{u} + \tilde{u}^2 + \bar{v}^2 + 2\bar{v}\tilde{v} + \tilde{v}^2 \tag{A.15}$$

To get the right hand side of equation (A.15) to be the same as the right hand side of (A.12) in order to compute $<q^2>$) from <u> and <v>, $<u'^2>$ and $<v'^2>$ are added and subtracted to the right-hand side of equation (A.15), yielding

$$\langle u\rangle^2 + \langle v\rangle^2 = \left[\bar{u}^2 + 2\bar{u}\tilde{u} + \langle u'^2\rangle\right] - \langle u'^2\rangle + \tilde{u}^2 + \left[\bar{v}^2 + 2\bar{v}\tilde{v} + \langle v'^2\rangle\right] - \langle v'^2\rangle + \tilde{v}^2 \tag{A.16}$$

grouping and recognizing terms corresponding to $<q^2>$ from equation (A.12) results in

$$\langle u\rangle^2 + \langle v\rangle^2 = \langle q^2\rangle - \langle u'^2\rangle + \tilde{u}^2 - \langle v'^2\rangle + \tilde{v}^2 \tag{A.17}$$

expanding u' and v' in terms of periodic and random components leads to

$$\langle u\rangle^2 + \langle v\rangle^2 = \langle q^2\rangle - \langle \tilde{u}^2 + 2\tilde{u}\hat{u} + \hat{u}^2\rangle + \tilde{u}^2 - \langle \tilde{v}^2 + 2\tilde{v}\hat{v} + \hat{v}^2\rangle + \tilde{v}^2 \tag{A.18}$$

using (A.9)

$$\langle u\rangle^2 + \langle v\rangle^2 = \langle q^2\rangle - \tilde{u}^2 - 2\tilde{u}\langle\hat{u}\rangle - \langle\hat{u}^2\rangle + \tilde{u}^2 - \tilde{v}^2 - 2\tilde{v}\langle\hat{v}\rangle - \langle\hat{v}^2\rangle + \tilde{v}^2 \tag{A.19}$$

using (A.10) and canceling terms of equal magnitude but opposite sign results in

$$\langle u \rangle^2 + \langle v \rangle^2 = \langle q^2 \rangle - \langle \hat{u}^2 \rangle - \langle \hat{v}^2 \rangle \tag{A.20}$$

which yields the equation needed to calculate $<q^2>$ using the conditional quantities provided in Greenblatt's data set

$$\boxed{\langle q^2 \rangle = \langle u \rangle^2 + \langle v \rangle^2 + \langle \hat{u}^2 \rangle + \langle \hat{v}^2 \rangle} \tag{A.21}$$

References

---

[1] Greenblatt, D., Paschal, K., Yao, C., Harris, J., "A Separation Control CFD Validation Test Case Part 2. Zero Efflux Oscillatory Blowing", AIAA-2005-0485 43rd American Institute of Aeronautics and Astronautics Aerospace Sciences Meeting and Exhibit, Reno, NV 2005.

REPORT DOCUMENTATION PAGE

Form Approved
OMB No. 0704-0188

The public reporting burden for this collection of information is estimated to average 1 hour per response, including the time for reviewing instructions, searching existing data sources, gathering and maintaining the data needed, and completing and reviewing the collection of information. Send comments regarding this burden estimate or any other aspect of this collection of information, including suggestions for reducing this burden, to Department of Defense, Washington Headquarters Services, Directorate for Information Operations and Reports (0704-0188), 1215 Jefferson Davis Highway, Suite 1204, Arlington, VA 22202-4302. Respondents should be aware that notwithstanding any other provision of law, no person shall be subject to any penalty for failing to comply with a collection of information if it does not display a currently valid OMB control number.
PLEASE DO NOT RETURN YOUR FORM TO THE ABOVE ADDRESS.

1. REPORT DATE *(DD-MM-YYYY)*
01- 07 - 2007

2. REPORT TYPE
Contractor Report

3. DATES COVERED *(From - To)*

4. TITLE AND SUBTITLE
Velocity-Field Measurements of an Axisymmetric Separated Flow Subjected to Amplitude-Modulated Excitation

5a. CONTRACT NUMBER

5b. GRANT NUMBER
NNL05AA11H

5c. PROGRAM ELEMENT NUMBER

6. AUTHOR(S)
Trosin, Barry James

5d. PROJECT NUMBER

5e. TASK NUMBER

5f. WORK UNIT NUMBER
561581.02.08.07

7. PERFORMING ORGANIZATION NAME(S) AND ADDRESS(ES)
NASA Langley Research Center
Hampton, VA 23681-2199

Michigan State University
Department of Mechanical Engineering
East Lansing, MI 48824

8. PERFORMING ORGANIZATION REPORT NUMBER

9. SPONSORING/MONITORING AGENCY NAME(S) AND ADDRESS(ES)
National Aeronautics and Space Administration
Washington, DC 20546-0001

10. SPONSOR/MONITOR'S ACRONYM(S)
NASA

11. SPONSOR/MONITOR'S REPORT NUMBER(S)
NASA/CR-2007-214889

12. DISTRIBUTION/AVAILABILITY STATEMENT
Unclassified - Unlimited
Subject Category 71
Availability: NASA CASI (301) 621-0390

13. SUPPLEMENTARY NOTES
Langley Technical Monitor: William M. Humphreys
An electronic version can be found at http://ntrs.nasa.gov

14. ABSTRACT

Active flow control was applied at the point of separation of an axisymmetric, backward-facing-step flow. The control was implemented by employing a Helmholtz resonator that was externally driven by an amplitude-modulated, acoustic disturbance from a speaker located upsteam of the wind tunnel. The velocity field of the separating/reattaching flow region downstream of the step was characterized using hotwire velocity measurements with and without flow control. Conventional statistics of the data reveal that the separating/reattaching flow is affected by the imposed forcing. Triple decomposition along with conditional averaging was used to distinguish periodic disturbances from random turbulence in the fluctuating velocity component. A significant outcome of the present study is that it demonstrates that amplitude-modulated forcing of the separated flow alters the flow in the same manner as the more conventional method of periodic excitation.

15. SUBJECT TERMS
Pressure measurements; Flow excitation; Separated flows

16. SECURITY CLASSIFICATION OF:			17. LIMITATION OF ABSTRACT	18. NUMBER OF PAGES	19a. NAME OF RESPONSIBLE PERSON
a. REPORT	b. ABSTRACT	c. THIS PAGE			STI Help Desk (email: help@sti.nasa.gov)
U	U	U	UU	110	19b. TELEPHONE NUMBER *(Include area code)* (301) 621-0390

Standard Form 298 (Rev. 8-98)
Prescribed by ANSI Std. Z39.18